
Causal Attribution via Activation Patching

Amirmohammad Izadi*, Mohammadali Banayeezade*, Alireza Mirrokni*, Hosein Hasani*,
Mobin Bagherian, Faridoun Mehri, and Mahdieh Soleymani Baghshah

Sharif University of Technology

Abstract

Attribution methods for Vision Transformers (ViTs) aim to identify image regions that influence model predictions, but producing faithful and well-localized attributions remains challenging. Existing gradient-based and perturbation-based techniques often fail to isolate the causal contribution of internal representations associated with individual image patches. The key challenge is that class-relevant evidence is formed through interactions between patch tokens across layers, and input-level perturbations can be poor proxies for patch importance, since they may fail to reconstruct the internal evidence actually used by the model. We propose **Causal Attribution via Activation Patching (CAAP)**, which estimates the contribution of individual image patches to the ViT’s prediction by directly intervening on internal activations rather than using learned masks or synthetic perturbation patterns. For each patch, CAAP inserts the corresponding source-image activations into a neutral target context over an intermediate range of layers and uses the resulting target-class score as the attribution signal. The resulting attribution map reflects the causal effect of patch-associated internal representations on the model’s prediction. The causal intervention serves as a principled measure of patch influence by capturing class-relevant evidence after initial representation formation, while avoiding late-layer global mixing that can reduce spatial specificity. Across multiple ViT backbones and standard metrics, CAAP significantly outperforms existing methods and produces more faithful and localized attributions.

1 Introduction

Vision Transformers (ViTs) have become a dominant architecture for image recognition and representation learning, including supervised and foundation models such as ViT [34], CLIP [27], DINOv2 [22] and DeiT3 [37]. Their patch-based tokenization and global self-attention naturally motivate attribution methods that operate at the patch or token level rather than on individual pixels [9]. Input attribution methods aim to quantify how specific input features contribute to a model’s prediction and are commonly used to analyze model behavior, identify reliance on spurious cues, and compare learned representations [29]. Existing attribution approaches for vision models include gradient-based methods [31, 35, 30], perturbation-based methods [25, 40, 8], and combined methods that use gradients and attention [7, 26]. Despite advances, there is still room for improvement in producing faithful and well-localized attributions for ViTs.

Perturbation-based methods, including masking approaches in input or token space [25, 40, 8], estimate importance by measuring prediction changes under interventions and therefore provide a causal notion of attribution. However, they have important practical limitations. Deletion-based evaluation does not account for redundancy across patches: when multiple patches encode similar class evidence, removing one patch may cause little change in the output, leading to an underestimation of its importance. Insertion-based approaches face a different limitation. Inserting a single patch into an otherwise blank or blurred input fails to reproduce the functional role that the patch plays within the full image context. Moreover, input-space perturbations can introduce distribution shift, and existing methods often rely on input masks [10, 40] or optimization-based [38] surrogates that may deviate from the model’s native internal decision variables. These limitations motivate causal attribution methods that operate directly on internal representations rather than on raw input [6, 42].

*Equal contribution.

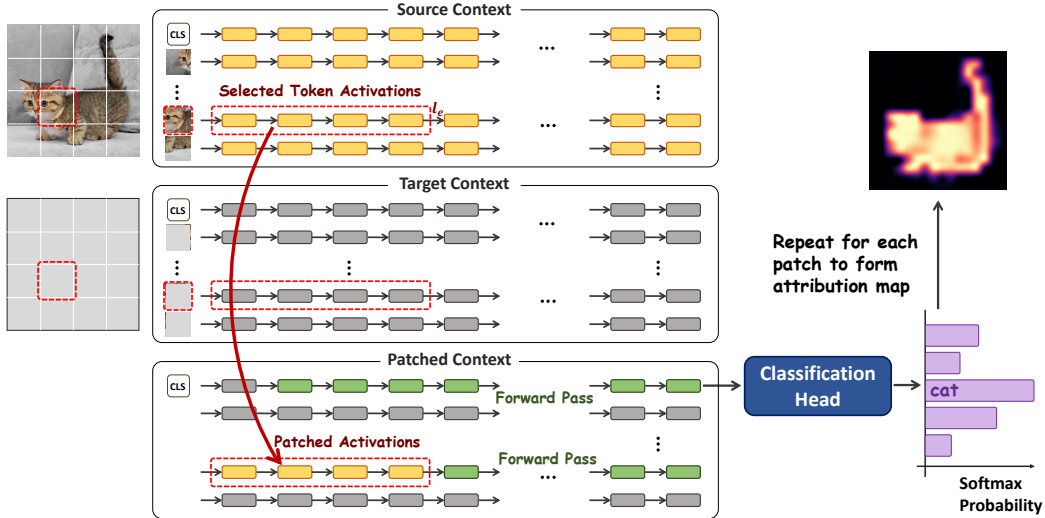


Figure 1: Overview of CAAP. Given a source image (top) and a blank target image (middle), we extract internal activations from the source image corresponding to a selected patch and a specified range of layers. These activations are injected into the target context to form a patched context (bottom), while all other activations remain unchanged. A forward pass on the patched sequence produces a class score for the CLS token (green), which measures the causal effect of the selected patch on the target prediction. Repeating this intervention for all patches yields a patch-level attribution.

In this work, we propose **Causal Attribution via Activation Patching (CAAP)**, a novel attribution method motivated by mechanistic interpretability. CAAP measures attribution by intervening on hidden activations of a trained ViT. For each patch, we insert the corresponding source-image activations into a neutral blank context and use the resulting target-class score as the attribution signal. Crucially, we apply activation patching over an intermediate layer range: late enough that patch representations contain enriched class-relevant object information, but early enough to avoid late-layer contextual mixing that can reduce spatial specificity. This design allows CAAP to better isolate the causal contribution of class-relevant patch representations to the final prediction.

Causal intervention offers a practical advantage for CAAP over existing attribution techniques. It assigns attribution scores directly based on information already encoded in the internal representations of tokens, rather than approximating relevance through gradients, attention weights, or learned saliency masks. The procedure can be efficiently parallelized, enabling practical patch-level attribution for large ViT backbones. Empirical results across multiple Vision Transformer backbones show that our method significantly outperforms existing approaches, achieving state-of-the-art results on deletion, insertion, and foreground and background localization metrics. Quantitative and qualitative results demonstrate that this method provides a reliable and effective mechanism for spatial attribution in Vision Transformers, introducing a new methodological paradigm for attribution, based on causal interventions.

2 Preliminaries

2.1 Problem Definition

We consider an image classification model f that maps an input image $x \in \mathbb{R}^{C \times H \times W}$ to a vector of class scores $f(x) \in \mathbb{R}^K$, where K is the number of classes. For a target class y , we denote the corresponding prediction score by $p(y | x) = f(x)_y$. The image x is partitioned into a set of non-overlapping visual patches $\mathcal{P} = \{p_1, \dots, p_N\}$, where each patch corresponds to a spatial region in the input. The goal of visual attribution is to assign a scalar attribution score $A(p_i) \in \mathbb{R}$ to each patch p_i , measuring the contribution of that patch to the prediction $f(x)_y$. An attribution method produces an attribution map $A \in \mathbb{R}^N$ such that higher values indicate greater relevance to the target prediction.

2.2 Activation Patching

Let f be a neural network composed of L layers. For an input x , we denote by $h^l(x)$ the activation tensor at layer $l \in \{1, \dots, L\}$. Activation patching is an intervention-based procedure that modifies a forward pass by replacing selected internal activations of one input with those from another, while keeping all other computations

Algorithm 1: CAAP: Causal Attribution via Activation Patching

Input: Classifier f ; image x ; blank image x_0 ; target class y ; patch set $\mathcal{P} = \{p_1, \dots, p_N\}$; intervened layers \mathcal{L} ; selection operator $\mathcal{S}(\cdot)$.

Output: Patch attribution map $A \in \mathbb{R}^N$

Compute and cache activations $\{h^l(x)\}_{l=1}^L$ and $\{h^l(x_0)\}_{l=1}^L$;

for $i \leftarrow 1$ **to** N **do**

 Initialize patched context from target activations:

$$h^l(c^*) \leftarrow h^l(x_0), \quad \forall l \in \{1, \dots, L\}$$

 Replace source activations at selected indices:

$$h^l(c^*(p_i))_{\mathcal{S}(p_i)} \leftarrow h^l(x)_{\mathcal{S}(p_i)}, \quad \forall l \in \mathcal{L}$$

 Resume forward computation from layer $l_s + 1$ to L :

 Propagate the CLS token through all layers $l_s + 1, \dots, L$,
 and propagate the patched tokens $\mathcal{S}(p_i)$ through layers $l_e + 1, \dots, L$.

 Compute the target-class score:

$$A(p_i) \leftarrow f(c^*(p_i))_y.$$

return A ;

unchanged. We refer to the input providing the replaced activations as the source context c , and the input receiving these activations as the target context c' .

The patched context c^* is first initialized with the target context c' . Given a set of layers \mathcal{L} and selection operator \mathcal{S} over token indices, the patched context c^* is then constructed by setting

$$h^l(c^*)_{\mathcal{S}} = h^l(c)_{\mathcal{S}}, \quad h^l(c^*)_{-\mathcal{S}} = h^l(c')_{-\mathcal{S}}, \quad \forall l \in \mathcal{L}, \quad (1)$$

while all remaining activations are propagated according to the model’s standard forward computation. The model output $f(c^*)$ reflects the effect of intervening on the selected internal activations of c , enabling causal analysis of their influence on the final prediction.

3 Method

We propose CAAP for ViT models, a patch-level attribution method that assigns relevance scores by intervening on the internal activations of a trained classifier. Rather than measuring local sensitivity at the input level, CAAP quantifies the causal effect of internal representations associated with a visual patch on the final prediction. This addresses a core limitation of input-level insertion and deletion methods. Deletion can underestimate importance when class-relevant information is redundant and spread across multiple patches, while insertion into a blank image ignores token interactions across transformer layers.

Let x be the input image and x_0 a blank image of the same resolution, used as a neutral target context that contains no class-specific visual evidence. We treat x as the source context (c) and x_0 as the target context (c'). For each visual patch $p_i \in \mathcal{P}$, we identify the corresponding spatial indices in the activation tensors and define a patch selection operator $\mathcal{S}(p_i)$. For a chosen set of layers $\mathcal{L} = \{l_s, \dots, l_e\}$, the patched context $c^*(p_i)$ is constructed by replacing activations as

$$h^l(c^*(p_i))_{\mathcal{S}(p_i)} = h^l(x)_{\mathcal{S}(p_i)}, \quad h^l(c^*(p_i))_{-\mathcal{S}(p_i)} = h^l(x_0)_{-\mathcal{S}(p_i)}. \quad (2)$$

Starting from layer $l_s + 1$, we resume the forward computation by propagating the CLS token through all subsequent layers up to the output, and after layer $l_e + 1$ we also continue the forward computation for the patched tokens $\mathcal{S}(p_i)$ so that their residual streams are updated consistently with the intervened activations. The attribution score for patch p_i with respect to class y is defined as the prediction score obtained from the patched context,

$$A(p_i) = f(c^*(p_i))_y. \quad (3)$$

This score measures how predictive the contextualized token embedding associated with patch p_i is for the target class, by inserting it into a neutral context and observing its effect on the output. Repeating this procedure for all patches yields a patch-level attribution map over the input image. The overall procedure is summarized in Algorithm 1 and shown in Fig. 1.

3.1 Patch Selection Operator \mathcal{S}

In the naive implementation, the patch selection operator $\mathcal{S}(p_i)$ corresponds exactly to the patch p_i . However, patching a single token often does not transfer sufficient predictive information from the source context. To

account for spatial feature spread across neighboring tokens, we consider a padded variant in which $\mathcal{S}(p_i)$ includes the patch p_i and its immediate spatial neighbors. This choice preserves both contextual information and spatial locality, making the patch-level intervention a more faithful measure of localized contribution.

3.2 Choice of Intervened Layers \mathcal{L}

Vision Transformers build patch representations through repeated self-attention, causing each patch token to encode information aggregated from other patches. This perspective suggests distinguishing two representation regimes in ViTs [23]. First, patch tokens undergo a grouping process in which class-consistent and object-related features become organized across patches. Second, tokens increasingly encode broader context through interactions that may involve tokens from different objects or background regions. For most pretrained ViTs, intra-object grouping occurs in the early layers, while inter-object or background contextualization emerges in the later layers [23].

In the context of attribution, early-stage grouping is desirable because it strengthens class-related evidence by integrating dependencies between adjacent patches. In contrast, late-stage contextualization can reduce spatial specificity, as class-relevant evidence becomes entangled with global scene structure and background information. Therefore, a reasonable choice of \mathcal{L} is to include the early and intermediate layers, up to the point where background or other non-class-related features begin to mix into the patch representations. We next provide further insight into grouping and mixing mechanisms through the self-attention operation.

Consider a Vision Transformer with N patch tokens. Let $z_i^l \in \mathbb{R}^d$ denote the representation of patch i at layer l . In a single attention head, the attention update for patch i can be written as

$$\tilde{z}_i^{l+1} = \sum_{j=1}^N \alpha_{ij}^l v_j^l, \quad (4)$$

where v_j^l are value vectors derived from the token representations and α_{ij}^l are attention weights defined by

$$\alpha_{ij}^l = \frac{\exp(\langle q_i^l, k_j^l \rangle / \sqrt{d})}{\sum_{m=1}^N \exp(\langle q_i^l, k_m^l \rangle / \sqrt{d})}. \quad (5)$$

Let \mathcal{O} denote the set of patches belonging to the same object as patch i . The attention update can be decomposed as

$$\tilde{z}_i^{l+1} = \sum_{j \in \mathcal{O}} \alpha_{ij}^l v_j^l + \sum_{j \notin \mathcal{O}} \alpha_{ij}^l v_j^l. \quad (6)$$

We empirically show that in the early layers, where intra-object grouping occurs, the quantity $\mathbb{E}_{j \in \mathcal{O}}[\alpha_{ij}^l] - \mathbb{E}_{j \notin \mathcal{O}}[\alpha_{ij}^l]$ increases, while after the middle layers it decreases. This enrichment of intra-object grouping supports the motivation for layer-wise activation patching rather than input-level insertion. However, it also suggests that patching up to the final layer is not desirable, due to increasing extra-object contextualization. In practice, we select the intervened layers from the beginning up to $\lceil \frac{2}{3}L \rceil$, where patch representations contain strong object-level information while preserving spatial specificity.

3.3 Efficient Implementation

In transformer architectures, the hidden states at each layer are linearly projected to queries, keys, and values. To avoid recomputation of these vectors from hidden states during activation patching, we reuse the cached key and value projections associated with the intervened hidden states rather than recomputing them from the residual streams. Only the query vectors of the additional CLS tokens are computed dynamically. We next propose two practical ideas to further accelerate the intervention process.

3.3.1 Parallel computation over patches

The patch-wise formulation requires one forward pass per patch, which scales linearly with the number of tokens in the image. Since the intervention is defined on internal activations, we can compute all patch attribution scores in parallel within a single forward pass while preserving the same causal intervention. This construction exploits the structure of activation patching and is not applicable to input-space masking methods, which require independent forward passes for each modified input.

For the blank image x_0 , we perform a single forward pass once and cache its activations $\{h^l(x_0)\}_{l \in \mathcal{L}}$, which are reused for all image samples. Then, for each source image x , we run a standard forward pass and cache the

activations $\{h^l(x)\}_{l \in \mathcal{L}}$. We then build a patched computation that contains both activation sets. For each patch p_i , we introduce a dedicated classification token CLS_i with the same positional encoding as the original classification token. The attention mask is defined such that CLS_i attends to source activations at indices $\mathcal{S}(p_i)$ and to target activations at indices $\neg\mathcal{S}(p_i)$. No attention is allowed between different classification tokens, and only the CLS tokens are propagated through the remaining layers.

The class score produced by CLS_i for class y is equal to the attribution score in Eq. 3 obtained by patch-wise activation replacement for p_i . Hence, this construction yields the same attribution map while computing all patch scores in parallel. Therefore, the total computational cost per dataset sample consists of one forward pass for the source image, followed by a single forward pass with multiple CLS tokens. Since the additional computation arises only from extra query tokens with shared key–value attention, the cost is bounded by a small constant factor relative to a standard forward pass.

3.3.2 Precomputation of blank-context attention

Even in the parallel construction, a large fraction of the computation arises from attention between each classification token and patch tokens originating from the blank image x_0 . Let K_0^l and V_0^l denote the key and value matrices at layer l computed from x_0 . These quantities are fixed and do not depend on the source image x or on the selected patch p_i . In the patched context c^* , the update of each classification token CLS_i follows the same self-attention operation defined in Eqs. 4 and 5, with the query corresponding to CLS_i rather than a patch token. In this setting, keys and values are drawn either from source-patched tokens $j \in \mathcal{S}(p_i)$ or from blank-context tokens $j \notin \mathcal{S}(p_i)$.

Empirically, we observe that for blank patches the dot products $\langle q_{\text{CLS}}^c, k_{0,j}^l \rangle$ and $\langle q_{\text{CLS}}^{c^*(p_i)}, k_{0,j}^l \rangle$ are nearly identical across images and interventions. As a result, the attention distribution over blank tokens is effectively invariant to the inserted source activations. We therefore precompute, for each layer and head, the aggregated contribution of blank patches to the CLS update using the corresponding statistics from the blank context c' (see Appendix B.1 for more details). During attribution, we reuse these fixed quantities and compute only the terms involving source-patched tokens dynamically. This avoids repeated evaluation of dot products and attention weights for blank patches across images. In practice, this approximation does not reduce faithfulness or localization performance, while decreasing floating-point operations by approximately an order of magnitude.

4 Experiments

In this section we present qualitative and quantitative evaluations of our proposed ViT attribution method. We begin by defining the evaluation metrics used throughout the experiments, followed by a detailed description of the ViT models, datasets, and baseline methods. We then present the quantitative results and ablation studies analyzing the contribution of each component of our method.

4.1 Evaluation Metrics

We evaluate attribution maps using six metrics that assess two complementary aspects of quality: Faithfulness and Localization. Deletion AUC and Insertion AUC [25] are faithfulness measures; they test whether pixels ranked as important by the attribution are indeed the ones the model relies on. To obtain a single faithfulness metric, we also report Insertion–Deletion, defined as the difference between Insertion and Deletion AUC. AUPR_1 , AUPR_0 [19], and Pointing-Game (PG) [3] are localization measures; they quantify how well attribution mass concentrates on annotated foreground regions and avoids background regions.

Faithfulness metrics. Following the evaluation protocol of [25], given an attribution map A for an image x and corresponding class y , we sort pixels in descending order of A and perturb x accordingly. For Deletion, we progressively replace the top-ranked pixels with a constant reference value and track the target class score $f(\cdot)_y$; the area under this curve is Deletion AUC. For Insertion, we start from a blurred version of x and progressively reveal (unblur) the top-ranked pixels, again tracking $f(\cdot)_y$; the area under this curve is Insertion AUC. More faithful attributions yield lower Deletion AUC and higher Insertion AUC.

Localization metrics. Given a normalized attribution map $A \in [0, 1]^{H \times W}$ and a ground-truth binary mask $M \in \{0, 1\}^{H \times W}$, AUPR treats A as a pixel-wise confidence map and sweeps a threshold to form a precision–recall curve. AUPR_1 defines positives as foreground pixels, while AUPR_0 defines positives as background pixels by evaluating background confidence $1 - A$ against the inverted mask $1 - M$. PG [3] checks whether the maximum-attribution pixel $(i^*, j^*) = \arg \max_{i,j} A_{i,j}$ falls inside the annotated foreground region. The PG score is defined as the fraction of hits over all images. Higher AUPR_1 , AUPR_0 , and PG indicate better spatial alignment with the ground-truth regions.

Table 1: Faithfulness quantitative results on ImageNet for ViT-L/16 [34], CLIP-L/14 [27], DINOv2-L/14 [22], and DeiT3-L/16 [37]. Deletion (\downarrow), Insertion (\uparrow), and Ins–Del (\uparrow) are reported. Best is **bold**, second best is underlined in each column.

Method	ViT-L/16 [34]			CLIP-L/14 [27]			DINOv2-L/14 [22]			DeiT3-L/16 [37]		
	Del \downarrow	Ins \uparrow	Ins–Del \uparrow	Del \downarrow	Ins \uparrow	Ins–Del \uparrow	Del \downarrow	Ins \uparrow	Ins–Del \uparrow	Del \downarrow	Ins \uparrow	Ins–Del \uparrow
Grad-CAM [30]	48.99 \pm 1.22	70.40 \pm 1.08	21.40 \pm 1.17	46.74 \pm 1.14	73.19 \pm 0.85	26.46 \pm 1.07	49.36 \pm 1.20	76.01 \pm 1.11	26.65 \pm 1.00	<u>31.81</u> \pm 0.89	62.18 \pm 0.93	30.37 \pm 0.80
Rollout [1]	67.69 \pm 1.06	56.11 \pm 1.24	-11.58 \pm 1.03	60.08 \pm 1.05	64.90 \pm 1.00	4.82 \pm 0.99	63.10 \pm 1.16	73.97 \pm 1.20	10.86 \pm 0.81	58.80 \pm 1.04	53.27 \pm 1.04	-5.54 \pm 0.86
T-Attr [7]	53.99 \pm 1.21	68.75 \pm 1.08	14.77 \pm 1.10	50.20 \pm 1.14	72.35 \pm 0.90	22.15 \pm 1.02	63.23 \pm 1.14	73.82 \pm 1.20	10.59 \pm 0.86	37.36 \pm 1.00	66.48 \pm 0.96	29.12 \pm 0.92
ViT-CX [40]	<u>48.57</u> \pm 1.27	<u>71.36</u> \pm 1.10	<u>22.79</u> \pm 1.25	50.27 \pm 1.26	69.65 \pm 0.96	19.38 \pm 1.40	49.50 \pm 1.26	<u>78.02</u> \pm 1.12	<u>28.51</u> \pm 1.17	38.56 \pm 1.13	58.99 \pm 0.96	20.43 \pm 1.22
TAM [41]	49.86 \pm 1.26	69.52 \pm 1.11	19.71 \pm 1.25	46.25 \pm 1.17	73.69 \pm 0.88	27.44 \pm 1.12	54.83 \pm 2.08	77.52 \pm 1.59	22.68 \pm 1.55	35.88 \pm 1.04	<u>67.78</u> \pm 0.95	31.90 \pm 0.94
IxG+ [20]	64.75 \pm 1.27	59.21 \pm 1.19	-5.54 \pm 1.01	61.87 \pm 1.19	70.56 \pm 0.96	8.69 \pm 0.92	68.12 \pm 1.24	73.45 \pm 1.34	5.33 \pm 1.82	52.16 \pm 1.07	65.08 \pm 1.06	12.92 \pm 0.98
Libra IxG+ [21]	51.92 \pm 1.30	71.14 \pm 1.11	19.22 \pm 1.21	<u>44.27</u> \pm 1.16	<u>75.24</u> \pm 0.83	<u>30.97</u> \pm 1.08	60.80 \pm 1.22	74.99 \pm 1.21	14.18 \pm 1.71	33.72 \pm 1.00	69.49 \pm 0.90	35.77 \pm 0.93
MDA [38]	57.02 \pm 1.16	62.12 \pm 1.21	5.10 \pm 1.28	46.56 \pm 1.14	70.31 \pm 0.94	23.74 \pm 1.21	<u>49.20</u> \pm 1.21	76.95 \pm 1.16	27.75 \pm 1.07	47.49 \pm 1.03	54.52 \pm 1.01	7.02 \pm 1.06
MUTEX [18]	50.84 \pm 1.20	68.60 \pm 1.08	17.76 \pm 1.11	48.75 \pm 1.16	70.85 \pm 0.89	22.11 \pm 1.10	53.06 \pm 1.10	76.32 \pm 1.15	23.26 \pm 0.84	39.14 \pm 1.05	64.77 \pm 0.93	25.62 \pm 1.04
CAAP (Ours)	42.67 \pm 1.16	73.42 \pm 1.07	30.75 \pm 1.18	34.35 \pm 0.99	75.88 \pm 0.85	41.52 \pm 1.02	43.11 \pm 1.14	80.09 \pm 1.08	36.98 \pm 1.00	31.56 \pm 0.91	64.84 \pm 0.93	33.28 \pm 0.85

Table 2: Localization quantitative results on ImageNet for ViT-L/16 [34], CLIP-L/14 [27], DINOv2-L/14 [22], and DeiT3-L/16 [37]. AUPR₁ (\uparrow), AUPR₀ (\uparrow) and PG (\uparrow) are reported. Best is **bold**, second best is underlined in each column.

Method	ViT-L/16 [34]			CLIP-L/14 [27]			DINOv2-L/14 [22]			DeiT3-L/16 [37]		
	AUPR ₁ \uparrow	AUPR ₀ \uparrow	PG \uparrow	AUPR ₁ \uparrow	AUPR ₀ \uparrow	PG \uparrow	AUPR ₁ \uparrow	AUPR ₀ \uparrow	PG \uparrow	AUPR ₁ \uparrow	AUPR ₀ \uparrow	PG \uparrow
Grad-CAM [30]	52.75 \pm 2.12	78.83 \pm 2.10	50.00 \pm 4.42	53.34 \pm 2.05	75.29 \pm 2.27	<u>56.25</u> \pm 4.38	<u>50.10</u> \pm 2.11	<u>77.52</u> \pm 2.24	<u>43.75</u> \pm 4.38	<u>67.25</u> \pm 1.93	<u>85.64</u> \pm 1.86	<u>70.31</u> \pm 4.04
Rollout [1]	27.70 \pm 1.81	61.81 \pm 2.58	14.84 \pm 3.14	37.75 \pm 2.11	68.25 \pm 2.57	32.81 \pm 4.15	34.31 \pm 1.94	66.23 \pm 2.40	33.59 \pm 4.17	29.40 \pm 1.90	64.95 \pm 2.46	3.12 \pm 1.54
T-Attr [7]	38.74 \pm 1.91	72.64 \pm 2.41	20.31 \pm 3.56	51.00 \pm 1.70	75.27 \pm 2.35	40.62 \pm 4.34	40.23 \pm 2.32	72.22 \pm 2.16	36.72 \pm 4.26	60.90 \pm 1.71	81.13 \pm 1.99	34.38 \pm 4.20
ViT-CX [40]	<u>56.35</u> \pm 2.05	<u>78.97</u> \pm 2.22	<u>53.12</u> \pm 4.41	49.89 \pm 2.42	73.12 \pm 2.37	50.78 \pm 4.42	47.76 \pm 2.10	72.29 \pm 2.50	45.31 \pm 4.40	57.88 \pm 2.30	77.61 \pm 2.48	52.34 \pm 4.41
TAM [41]	49.52 \pm 1.71	74.59 \pm 2.48	41.41 \pm 4.35	<u>57.01</u> \pm 1.94	<u>77.66</u> \pm 2.30	54.69 \pm 4.40	43.62 \pm 1.89	72.91 \pm 2.45	34.38 \pm 4.20	62.34 \pm 1.86	82.35 \pm 2.00	57.03 \pm 4.38
IxG+ [20]	34.54 \pm 2.10	67.30 \pm 2.09	31.25 \pm 4.10	43.18 \pm 1.92	69.07 \pm 2.20	49.22 \pm 4.42	37.91 \pm 1.95	66.24 \pm 2.11	39.84 \pm 4.33	38.10 \pm 1.91	72.81 \pm 2.13	10.94 \pm 2.76
Libra IxG+ [21]	49.04 \pm 1.90	74.42 \pm 2.18	50.78 \pm 4.42	51.09 \pm 1.80	<u>77.90</u> \pm 2.15	36.72 \pm 4.26	38.73 \pm 2.03	71.19 \pm 2.17	35.94 \pm 4.24	56.53 \pm 1.68	80.70 \pm 2.09	39.06 \pm 4.31
MDA [38]	30.63 \pm 1.76	64.73 \pm 2.69	14.17 \pm 3.09	43.82 \pm 2.11	72.31 \pm 2.60	32.28 \pm 4.15	41.33 \pm 1.87	69.30 \pm 2.70	26.98 \pm 3.95	34.03 \pm 1.94	67.16 \pm 2.59	13.28 \pm 3.00
MUTEX [18]	46.61 \pm 1.87	73.48 \pm 2.51	35.16 \pm 4.22	46.81 \pm 2.02	75.21 \pm 2.39	39.84 \pm 4.33	43.96 \pm 2.14	77.74 \pm 2.16	35.16 \pm 4.22	51.46 \pm 2.04	77.87 \pm 2.28	48.44 \pm 4.42
CAAP (Ours)	63.40 \pm 2.01	83.40 \pm 1.99	73.44 \pm 3.90	66.42 \pm 1.78	84.86 \pm 1.89	74.22 \pm 3.87	52.76 \pm 1.86	76.68 \pm 2.17	41.41 \pm 4.35	71.21 \pm 1.86	86.93 \pm 1.85	82.81 \pm 3.33

4.2 Experiment Settings

Models and datasets. We conduct our main experiments on the ImageNet-1K (ILSVRC2012) validation set [28]. We evaluate four ViT-L models on ImageNet-1K: CLIP-L/14 [27], DINOv2-L/14 [22], ViT-L/16 [34], and DeiT3-L/16 [37]. For localization evaluation on ImageNet-1K, we use ImageNet-S [13] annotations and report AUPR₁, AUPR₀, and PG. Results for additional architectures are provided in Appendix A. To further validate our method, we additionally evaluate on ImageNet-Hard [36], Oxford-IIIT-Pet [24], and Food-101 [4]. For these datasets, we use a ViT-B/16 classifier initialized from pretrained weights. Results are reported on a random sample of 500 validation images per dataset.

Baselines. We compare our approach against a strong set of widely-used attribution baselines drawn from various attribution categories, including Grad-CAM [30], Attention Rollout [1], Transformer Attribution (T-Attr) [7], ViT-CX [40], TAM [41], IxG+ [20], Libra IxG+ [21], MDA [38], and MUTEX [18]. We evaluate all methods using the same protocol and metrics as our method.

4.3 Results

4.3.1 Quantitative

Faithfulness. Table 1 reports faithfulness metrics across four ViT models. Table 3 further presents the same faithfulness metrics on ImageNet-Hard [36] and Oxford-IIIT-Pet [24]. Our method consistently achieves the lowest Deletion AUC and the highest Insertion AUC on most backbones. In particular, our approach improves the Insertion–Deletion with a notable margin compared to prior methods, indicating that the regions ranked as important by our attribution maps more accurately reflect the model’s true decision-making process.

Localization. Localization results are reported in Table 2. Our method achieves the best overall performance across most models. In particular, the higher PG and AUPR₁ values indicate that the regions identified as most relevant are consistently located within the annotated foreground areas. Moreover, strong AUPR₀ scores demonstrate effective suppression of background activations. These results confirm that our approach produces spatially precise attribution maps that better align with ground-truth object regions. Further quantitative results are provided in Appendix A.1.

4.3.2 Qualitative

Qualitative results are provided in Figs 2 and 3. As illustrated, baseline methods often produce diffuse or fragmented attribution maps that extend beyond the target object into the background, or highlight only a small

Table 3: Faithfulness quantitative results on Oxford-IIIT-Pet [24], ImageNet-Hard [36], and Food-101 [4] for ViT-B/16. Deletion (\downarrow), Insertion (\uparrow), and Ins–Del (\uparrow) are reported. Best is **bold** and second best is underlined in each column.

Method	Oxford-IIIT-Pet [24]			ImageNet-Hard[36]			Food-101 [4]		
	Del \downarrow	Ins \uparrow	Ins–Del \uparrow	Del \downarrow	Ins \uparrow	Ins–Del \uparrow	Del \downarrow	Ins \uparrow	Ins–Del \uparrow
Grad-CAM [30]	61.95 \pm 1.08	78.41 \pm 0.77	16.46 \pm 1.23	14.66 \pm 0.89	26.04 \pm 1.15	11.38 \pm 1.11	51.84 \pm 1.26	62.08 \pm 1.00	10.25 \pm 1.22
Rollout [1]	73.84 \pm 0.90	72.15 \pm 0.83	-1.69 \pm 1.03	22.61 \pm 1.07	17.91 \pm 0.91	-4.70 \pm 0.97	60.70 \pm 1.07	54.77 \pm 1.02	-5.93 \pm 0.92
T-Attr [7]	53.37 \pm 0.99	84.32 \pm 0.61	30.95 \pm 0.99	12.86 \pm 0.79	27.41 \pm 1.14	14.55 \pm 1.01	41.23 \pm 1.07	65.52 \pm 1.00	24.30 \pm 1.00
ViT-CX [40]	<u>47.79</u> \pm 0.93	85.26 \pm 0.71	<u>37.47</u> \pm 1.03	14.14 \pm 0.78	25.76 \pm 1.19	11.62 \pm 1.12	37.62 \pm 0.96	66.34 \pm 1.07	28.71 \pm 1.11
TAM [41]	58.79 \pm 1.08	85.14 \pm 0.63	26.34 \pm 1.09	14.17 \pm 0.85	26.27 \pm 1.15	12.10 \pm 1.06	45.59 \pm 1.17	64.74 \pm 1.02	19.15 \pm 1.08
IxG+ [20]	76.15 \pm 1.05	79.06 \pm 0.79	2.92 \pm 1.08	15.77 \pm 0.98	23.89 \pm 1.16	8.12 \pm 1.14	50.27 \pm 1.32	63.05 \pm 1.01	12.78 \pm 1.13
Libra IxG+ [21]	54.72 \pm 1.07	<u>86.99</u> \pm 0.59	32.27 \pm 1.04	<u>10.90</u> \pm 0.73	31.64 \pm 1.29	20.74 \pm 1.21	<u>38.10</u> \pm 1.09	<u>69.47</u> \pm 1.00	<u>31.37</u> \pm 1.08
MDA [38]	61.82 \pm 1.22	75.18 \pm 0.98	13.36 \pm 1.51	19.69 \pm 0.98	21.30 \pm 1.03	1.61 \pm 1.03	49.54 \pm 1.22	60.99 \pm 1.18	11.45 \pm 1.19
MUTEX [18]	56.12 \pm 1.03	83.59 \pm 0.62	27.47 \pm 1.05	13.57 \pm 0.79	27.48 \pm 1.16	13.90 \pm 1.01	40.08 \pm 1.04	66.41 \pm 0.96	26.32 \pm 0.95
CAAP (Ours)	46.77 \pm 0.95	87.79 \pm 0.62	41.02 \pm 0.95	10.37 \pm 0.66	<u>30.70</u> \pm 1.24	<u>20.33</u> \pm 1.09	39.11 \pm 1.04	71.50 \pm 1.01	32.39 \pm 1.01

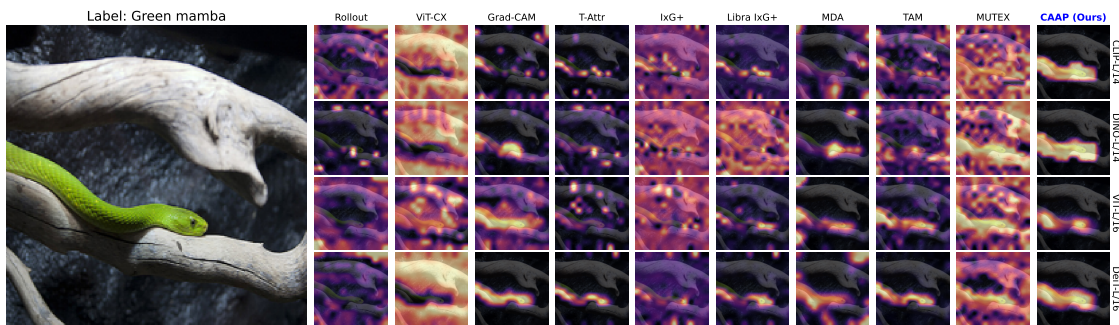


Figure 2: Qualitative attribution comparison between different methods for a representative ImageNet sample. CAAP produces more compact and well-localized attributions for the target class than the baselines. More examples are provided in the Appendix A.2.

subset of discriminative patches. In contrast, our method generates more compact, coherent, and semantically meaningful attributions that align closely with the target object. Specifically, our attributions better capture object boundaries and maintain consistency across patches, resulting in fewer spurious activations on irrelevant background regions. The improved localization quality observed in the visualizations is consistent with our superior AUPR₁, AUPR₀ and PG scores reported in Table 2. Additional qualitative results are provided in Appendix A.2.

4.4 Ablation Studies

We ablate three design choices in CAAP on ImageNet across all four ViT backbones: (i) the type of the target’s blank patches, (ii) the type of the selection operator, and (iii) the choice of intervened layers. Additional analysis regarding efficient implementation via precomputation of blank-context attention, comparison with input-based approaches and ablation analysis on convolutional architectures are provided in Appendices B.1, B.2 and B.3.

Target blank image type. We first ablate the type of blank target image patches used when constructing the patched target, varying the blank content among Black, Blur Noisy, Mean, Noisy, and White. Here, Mean fills the blanks with the dataset per-channel mean, Noisy fills them with i.i.d. Gaussian noise, and Blur Noisy first adds i.i.d. Gaussian noise to the target and then applies a blur filter on it. These choices span both in-distribution and out-of-distribution targets, since Mean matches dataset statistics while Black, White, and the noise-based variants introduce increasingly OOD blank content. Fig. 4 reports results on ImageNet across all four ViT backbones. Faithfulness is largely insensitive to this choice, as Insertion, Deletion, and Insertion–Deletion remain close across blank patch types for each model. AUPR₀ and AUPR₁ vary only marginally, while PG shows modest differences across backbones. We use White blanks as the default setting in all experiments.

Patch selection operator. We next ablate the spatial support of the intervention, motivated by the fact that ViT patch tokens absorb information from nearby patches via self-attention. Fig. 5 compares four neighborhood variants. Overall, the no-padding variant performs the worst, while all padded alternatives consistently improve both faithfulness and localization across different architectures. This result aligns with our selection operator

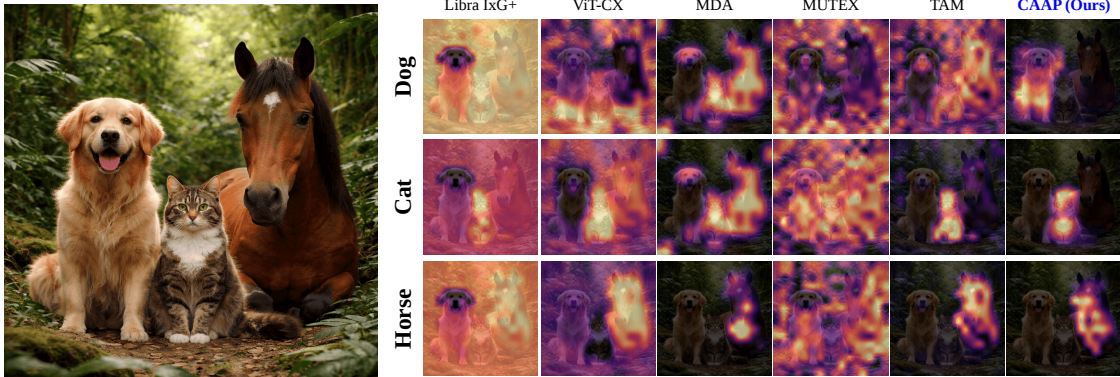


Figure 3: Qualitative attribution comparison in a representative image containing several objects using CLIP-L/14. CAAP produces compact and class-specific attributions aligned with the queried class. More examples are provided in the Appendix A.2.

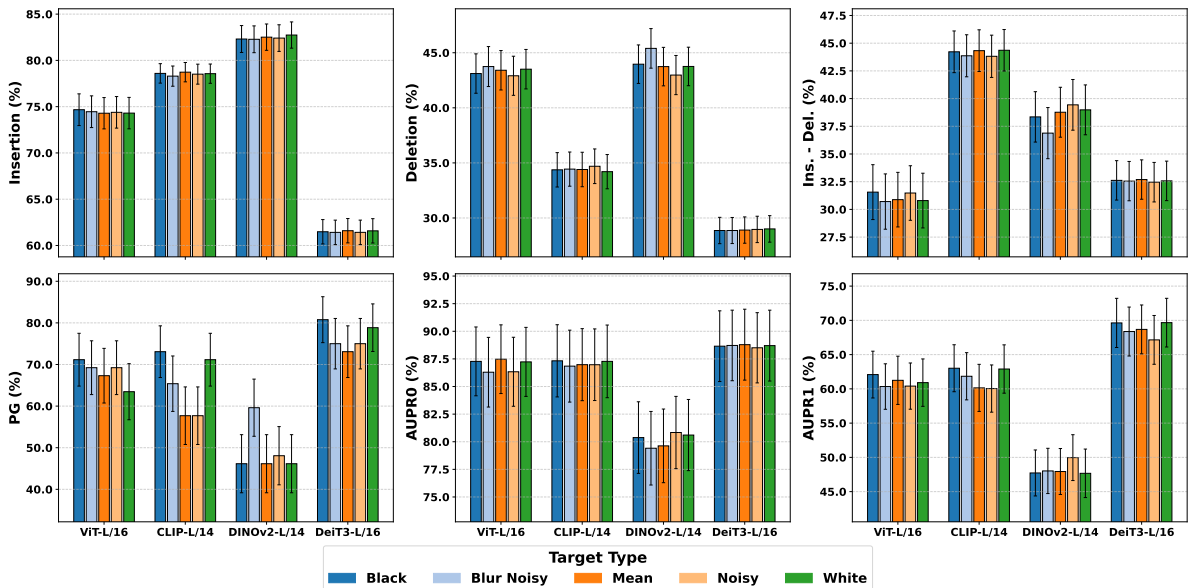


Figure 4: Target blank ablation on ImageNet across four ViT backbones. The type of target blank patches is varied (Black, Blur, Noisy Mean, Noisy, White), and faithfulness (Insertion, Deletion, Ins–Del) and localization (PG, AUPR₁, AUPR₀) are reported.

design (Section 3.1), confirming that because features spread spatially, patching a single token often misses context, and spatial padding improves attribution quality. We use the Radius-1 Box setting, which includes a 3×3 patch region, as the default in our experiments.

Choice of intervened layers. To analyze the effect of layer depth, we first examine attention patterns that govern information flow (Section 3.2). Fig. 6 shows the mean intra- and extra-object attention weights across layers, indicating that $\mathbb{E}_i[\mathbb{E}_{j \in \mathcal{O}}[\alpha_{ij}^l] - \mathbb{E}_{j \notin \mathcal{O}}[\alpha_{ij}^l]]$ peaks in the middle layers. To identify the optimal patching depth, we execute a cumulative layer sweep (Fig. 7), progressively patching all transformer blocks from the first up to a chosen cutoff layer. Across all ViT backbones, faithfulness consistently peaks at intermediate layers; interventions on early blocks mainly inject low-level features with limited class evidence, while extending patching into later blocks reduces reliability, as late representations are dominated by global mixing and weaker spatial specificity. Based on this observation, which aligns with the analysis in Section 3.2, we fix $l_e = \lceil \frac{2}{3}L \rceil$ as the default setting for all architectures, as it balances intra-object grouping and extra-object contextualization and is near-optimal across models.

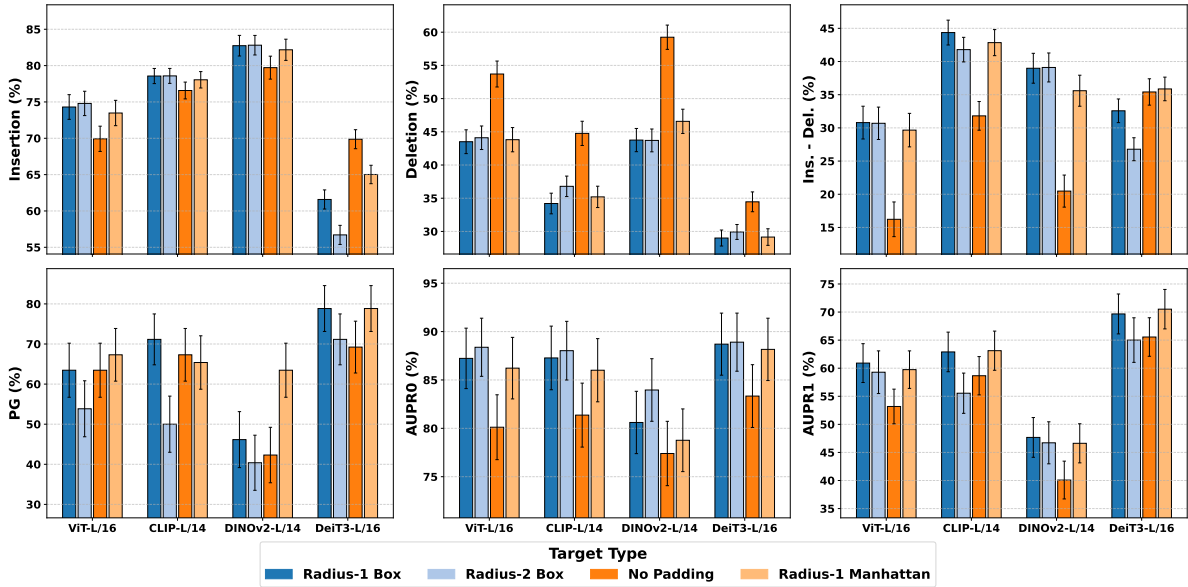


Figure 5: Selection operator ablation on ImageNet across four ViT backbones. The spatial support of the selection operator is varied by considering different neighborhood variants (No Padding, Radius-1 Box, Radius-2 Box, Radius-1 Manhattan), and faithfulness (Insertion, Deletion, Ins-Del) and localization (PG, $AUPR_1$, $AUPR_0$) are reported.

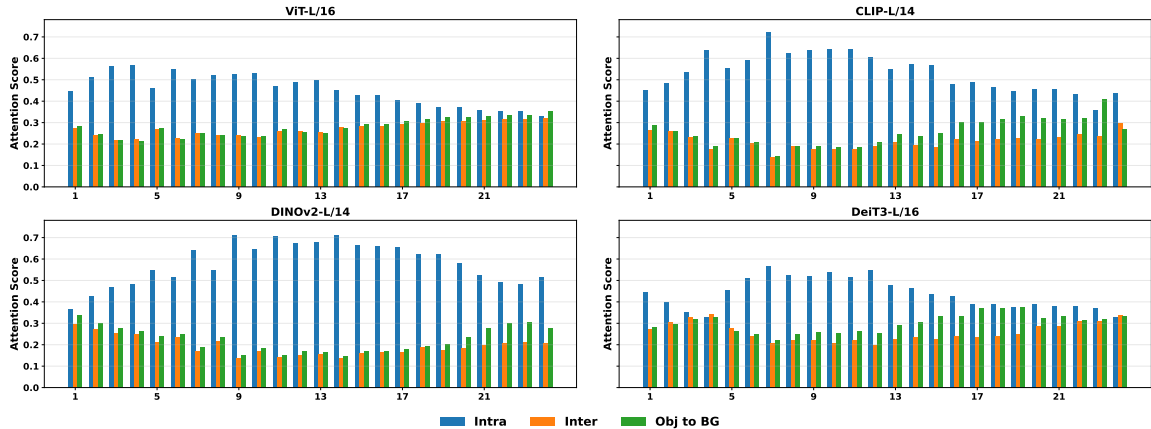


Figure 6: Mean attention weights across layers for different region pairs: intra-object (blue), inter-object (orange), and object-to-background (green). In early layers, intra-object attention increases and dominates, indicating strong object-level grouping. Around the middle layers, this gap reaches its peak. In later layers, intra-object attention decreases while object-to-background attention increases, reflecting growing extra-object contextualization and reduced spatial specificity.

5 Related Work

We review prior work on explaining Vision Transformers (ViTs) through three commonly used sources of explanatory signal: gradients, attention, and interventions based on perturbations.

Gradient-based attribution. Gradient-based approaches estimate relevance using local sensitivity of the class score with respect to inputs or intermediate features. Representative methods include Input \times Gradient and Integrated Gradients [31, 35], with noise-reduction variants such as SmoothGrad [33]. CAM-style localization derives class-discriminative maps from gradient-weighted features (Grad-CAM) and its extensions such as Grad-CAM++ and Score-CAM [30, 5, 39]. For ViTs, LibraGrad shows that architectural components can induce imbalanced gradient flow and proposes a post-hoc correction that improves patch-level attribution, and layer-aggregation variants such as IxG+ further strengthen explanations by combining layer-wise signals [21, 20].

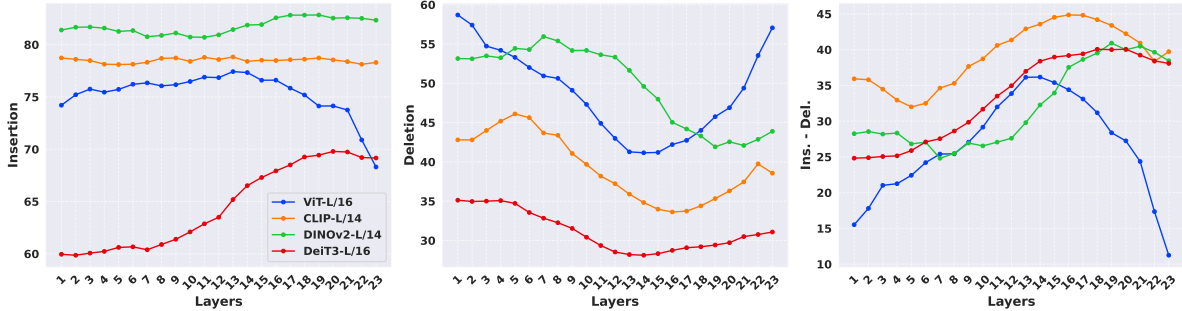


Figure 7: Intervention depth ablation on ImageNet using ViT backbones. For every cutoff point, we intervene on all transformer blocks from the initial layer up to that point and measure faithfulness metrics.

Attention-based attribution. Because ViTs rely on self-attention, many explanations derive saliency from attention weights and their compositions. Attention Flow and related rollout-style approaches compose attention across layers to propagate token influence [1]. However, attention weights alone do not necessarily align with causal importance [16, 17], motivating approaches that incorporate class information. Transformer Attribution propagates relevance through attention blocks using gradient-informed updates [7], and AttCAT combines features, gradients, and attention to produce token-level explanations [26]. Transition Attention Maps (TAM) models information flow through attention as a Markov process [41], while Grad-SAM leverages gradient self-attention maps to highlight influential inputs within attention units [2]. Graph-structured attention explanations also exist; MUTEX constructs a multiplex network over attention patterns across layers to generate patch heatmaps [18].

Perturbation-based attribution and masking in ViTs. Perturbation approaches estimate importance by modifying inputs or tokens and observing output changes. RISE aggregates responses over randomized masks [25], and optimization-based masking seeks minimally sufficient regions [11, 12]. For ViTs, ViT-CX builds causal explanations by masking patch embeddings and aggregating their effects on predictions [40], and Transformer Input Sampling (TIS) perturbs by sampling or dropping input tokens to avoid introducing replacement artifacts [10]. AtMan probes relevance by manipulating attention interactions efficiently [8]. Metric-Driven Attributions (MDA) directly optimizes attributions to score well under faithfulness metrics such as insertion and deletion [38].

Causal interventions and activation patching. Causal viewpoints formalize attribution as the effect of interventions rather than local sensitivity [6]. In mechanistic interpretability, activation patching (interchange interventions or causal tracing) replaces internal activations from a source run into a target run while keeping the remaining computation fixed, enabling direct tests of which internal representations carry information used for a prediction [42].

6 Discussion

CAAP reframes visual attribution in Vision Transformers as a causal intervention problem at the level of internal representations. Instead of relying on gradients, attention weights, or input-space perturbation, it measures the effect of replacing patch-specific activations within a controlled target context. This design directly evaluates how contextualized token embeddings influence the class score. By intervening at intermediate layers, CAAP captures class-relevant evidence after early object grouping while avoiding late-stage global mixing that weakens spatial specificity. In this sense, the method connects mechanistic activation patching with spatial attribution and provides a principled alternative to proxy-based explanations.

Empirically, CAAP improves faithfulness across multiple backbones, including CLIP, DINOv2, ViT, and DeiT3, by achieving lower Deletion AUC and higher Insertion AUC. Localization metrics such as $AUPR_1$, $AUPR_0$, and Pointing Game also improve, indicating that patch-level interventions better align with object regions rather than highlighting only a few highly discriminative patches. These results suggest that activation patching is not only a well-founded causal probe, but also an effective and scalable tool for identifying spatial evidence in ViTs. However, this method also has limitations, as it is largely fitted to transformer architectures. The activation patching reflects marginal patch effects and does not completely model higher-order interactions between patches. Extending the approach beyond this setting, including to other architectures or tasks such as multimodal or generative models, remains an open direction.

References

- [1] Samira Abnar and Willem Zuidema. Quantifying attention flow in transformers. In *Proceedings of the 58th Annual Meeting of the Association for Computational Linguistics*, pages 4190–4197, 2020. doi: 10.18653/v1/2020.acl-main.385. URL <https://aclanthology.org/2020.acl-main.385/>.
- [2] Oren Barkan, Edan Haulon, Avi Caciularu, Ori Katz, Itzik Malkiel, Omri Armstrong, and Noam Koenigstein. Grad-sam: Explaining transformers via gradient self-attention maps. In *Proceedings of the 30th ACM International Conference on Information and Knowledge Management (CIKM)*, pages 2882–2887, 2021. doi: 10.1145/3459637.3482126.
- [3] Amy Bearman, Olga Russakovsky, Vittorio Ferrari, and Li Fei-Fei. What’s the point: Semantic segmentation with point supervision, 2016. URL <https://arxiv.org/abs/1506.02106>.
- [4] Lukas Bossard, Matthieu Guillaumin, and Luc Van Gool. Food-101 – mining discriminative components with random forests. In *European Conference on Computer Vision*, 2014.
- [5] Aditya Chattopadhyay, Anirban Sarkar, Prantik Howlader, and Vineeth N. Balasubramanian. Grad-cam++: Improved visual explanations for deep convolutional networks, 2017. URL <https://arxiv.org/abs/1710.11063>.
- [6] Aditya Chattopadhyay, Anirban Sarkar, Prantik Howlader, and Vineeth N. Balasubramanian. Neural network attributions: A causal perspective. In *Proceedings of ICML*, 2019. URL <https://proceedings.mlr.press/v97/chatopadhyay19a.html>.
- [7] Hila Chefer, Shir Gur, and Lior Wolf. Transformer interpretability beyond attention visualization. In *Proceedings of the IEEE/CVF Conference on Computer Vision and Pattern Recognition (CVPR)*, pages 782–791, 2021.
- [8] Mayukh Deb, Björn Deiseroth, Samuel Weinbach, Patrick Schramowski, and Kristian Kersting. Atman: Understanding transformer predictions through memory efficient attention manipulation. *arXiv preprint arXiv:2301.08110*, 2023. URL <https://arxiv.org/abs/2301.08110>.
- [9] Alexey Dosovitskiy, Lucas Beyer, Alexander Kolesnikov, Dirk Weissenborn, Xiaohua Zhai, Thomas Unterthiner, Mostafa Dehghani, Matthias Minderer, Georg Heigold, Sylvain Gelly, Jakob Uszkoreit, and Neil Houlsby. An image is worth 16x16 words: Transformers for image recognition at scale, 2021. URL <https://arxiv.org/abs/2010.11929>.
- [10] Alexandre Englebert, Sédrick Stassin, Géraldine Nanfack, Sidi Ahmed Mahmoudi, Xavier Siebert, Olivier Cornu, and Christophe De Vleeschouwer. Explaining through transformer input sampling. In *Proceedings of the IEEE/CVF International Conference on Computer Vision Workshops (ICCVW)*, 2023. URL https://openaccess.thecvf.com/content/ICCV2023W/NIVT/html/Englebert_Explaining_Through_Transformer_Input_Sampling_ICCVW_2023_paper.html.
- [11] Ruth C. Fong and Andrea Vedaldi. Interpretable explanations of black boxes by meaningful perturbation. In *Proceedings of ICCV*, 2017. URL <https://www.robots.ox.ac.uk/~vgg/publications/2017/Fong17/>.
- [12] Ruth C. Fong, Mandela Patrick, and Andrea Vedaldi. Understanding deep networks via extremal perturbations and smooth masks. In *Proceedings of ICCV*, 2019.
- [13] Shanghua Gao, Zhong-Yu Li, Ming-Hsuan Yang, Ming-Ming Cheng, Junwei Han, and Philip Torr. Large-scale unsupervised semantic segmentation. *IEEE Transactions on Pattern Analysis and Machine Intelligence*, 45(6):7457–7476, 2023. doi: 10.1109/TPAMI.2022.3218275. URL <https://doi.org/10.1109/TPAMI.2022.3218275>.
- [14] Kaiming He, X. Zhang, Shaoqing Ren, and Jian Sun. Deep residual learning for image recognition. *2016 IEEE Conference on Computer Vision and Pattern Recognition (CVPR)*, pages 770–778, 2015. URL <https://api.semanticscholar.org/CorpusID:206594692>.
- [15] Gao Huang, Zhuang Liu, and Kilian Q. Weinberger. Densely connected convolutional networks. *2017 IEEE Conference on Computer Vision and Pattern Recognition (CVPR)*, pages 2261–2269, 2016. URL <https://api.semanticscholar.org/CorpusID:9433631>.
- [16] Sarthak Jain and Byron C. Wallace. Attention is not explanation. In *Proceedings of NAACL*, 2019. URL <https://aclanthology.org/N19-1357/>.

- [17] Goro Kobayashi, Tatsuki Kuribayashi, Sho Yokoi, and Kentaro Inui. Attention is not only a weight: Analyzing transformers with vector norms. In *Proceedings of EMNLP*, pages 7057–7075, 2020.
- [18] Michele Marchetti, Davide Traini, Domenico Ursino, and Luca Virgili. Multiplex network-based representation of vision transformers for visual explainability. *Neural Computing and Applications*, 37(29):24385–24420, 2025. doi: 10.1007/s00521-025-11591-x. URL <https://doi.org/10.1007/s00521-025-11591-x>.
- [19] Ran Margolin, Lihi Zelnik-Manor, and Ayellet Tal. How to evaluate foreground maps? In *CVPR*, 2014.
- [20] Faridoun Mehri, Mohsen Fayyaz, Mahdiah Soleymani Baghshah, and Mohammad Taher Pilehvar. SkipPLUS: Skip the first few layers to better explain vision transformers. In *Proceedings of the IEEE/CVF Conference on Computer Vision and Pattern Recognition (CVPR) Workshops*, pages 204–215, June 2024. doi: 10.1109/CVPRW63382.2024.00025. URL https://openaccess.thecvf.com/content/CVPR2024W/TCV2024/html/Mehri_SkipPLUS_Skip_the_First_Few_Layers_to_Better_Explain_Vision_CVPRW_2024_paper.html.
- [21] Faridoun Mehri, Mahdiah Soleymani Baghshah, and Mohammad Taher Pilehvar. Libragrad: Balancing gradient flow for universally better vision transformer attributions. In *Proceedings of the IEEE/CVF Conference on Computer Vision and Pattern Recognition (CVPR)*, pages 67–78, June 2025.
- [22] Maxime Oquab, Timothée Darcet, Théo Moutakanni, Huy Vo, Marc Szafraniec, Vasil Khalidov, Pierre Fernandez, Daniel Haziza, Francisco Massa, Alaaeldin El-Nouby, Mahmoud Assran, Nicolas Ballas, Wojciech Galuba, Russell Howes, Po-Yao Huang, Shang-Wen Li, Ishan Misra, Michael Rabbat, Vasu Sharma, Gabriel Synnaeve, Hu Xu, Hervé Jegou, Julien Mairal, Patrick Labatut, Armand Joulin, and Piotr Bojanowski. Dinov2: Learning robust visual features without supervision, 2024. URL <https://arxiv.org/abs/2304.07193>.
- [23] Xu Pan, Aaron Philip, Ziqian Xie, and Odell Schwartz. Dissecting query-key interaction in vision transformers. In *The Thirty-eighth Annual Conference on Neural Information Processing Systems*, 2024. URL <https://openreview.net/forum?id=dIktpSgK4F>.
- [24] Omkar M. Parkhi, Andrea Vedaldi, Andrew Zisserman, and C. V. Jawahar. Cats and dogs. In *IEEE Conference on Computer Vision and Pattern Recognition (CVPR)*, 2012.
- [25] Vitali Petsiuk, Abir Das, and Kate Saenko. Rise: Randomized input sampling for explanation of black-box models. In *BMVC*, 2018.
- [26] Yao Qiang, Deng Pan, Chengyin Li, Xin Li, Rhongho Jang, and Dongxiao Zhu. Attcatt: Explaining transformers via attentive class activation tokens. In *Advances in Neural Information Processing Systems (NeurIPS)*, 2022.
- [27] Alec Radford, Jong Wook Kim, Chris Hallacy, Aditya Ramesh, Gabriel Goh, Sandhini Agarwal, Girish Sastry, Amanda Askell, Pamela Mishkin, Jack Clark, Gretchen Krueger, and Ilya Sutskever. Learning transferable visual models from natural language supervision, 2021. URL <https://arxiv.org/abs/2103.00020>.
- [28] Olga Russakovsky, Jia Deng, Hao Su, Jonathan Krause, Sanjeev Satheesh, Sean Ma, Zhiheng Huang, Andrej Karpathy, Aditya Khosla, Michael Bernstein, Alexander C. Berg, and Li Fei-Fei. Imagenet large scale visual recognition challenge, 2015. URL <https://arxiv.org/abs/1409.0575>.
- [29] Wojciech Samek, Grégoire Montavon, Sebastian Lapuschkin, Christopher J. Anders, and Klaus-Robert Müller. Explaining deep neural networks and beyond: A review of methods and applications. *Proceedings of the IEEE*, 109(3):247–278, 2021.
- [30] Ramprasaath R. Selvaraju, Michael Cogswell, Abhishek Das, Ramakrishna Vedantam, Devi Parikh, and Dhruv Batra. Grad-cam: Visual explanations from deep networks via gradient-based localization. *International Journal of Computer Vision*, 128(2):336–359, 2019. doi: 10.1007/s11263-019-01228-7. URL <https://doi.org/10.1007/s11263-019-01228-7>.
- [31] Avanti Shrikumar, Peyton Greenside, Anna Shcherbina, and Anshul Kundaje. Not just a black box: Learning important features through propagating activation differences, 2016. URL <https://arxiv.org/abs/1605.01713>.
- [32] Karen Simonyan and Andrew Zisserman. Very deep convolutional networks for large-scale image recognition. *CoRR*, abs/1409.1556, 2014. URL <https://api.semanticscholar.org/CorpusID:14124313>.

- [33] Daniel Smilkov, Nikhil Thorat, Been Kim, Fernanda Viégas, and Martin Wattenberg. Smoothgrad: removing noise by adding noise, 2017. URL <https://arxiv.org/abs/1706.03825>.
- [34] Andreas Steiner, Alexander Kolesnikov, Xiaohua Zhai, Ross Wightman, Jakob Uszkoreit, and Lucas Beyer. How to train your vit? data, augmentation, and regularization in vision transformers, 2021. URL <https://arxiv.org/abs/2106.10270>.
- [35] Mukund Sundararajan, Ankur Taly, and Qiqi Yan. Axiomatic attribution for deep networks. In *Proceedings of the 34th International Conference on Machine Learning (ICML)*, pages 3319–3328. PMLR, 2017.
- [36] Mohammad Reza Taesiri, Giang Nguyen, Sarra Habchi, Cor-Paul Bezemer, and Anh Nguyen. Imagenet-hard: The hardest images remaining from a study of the power of zoom and spatial biases in image classification, 2023. URL <https://arxiv.org/abs/2304.05538>.
- [37] Hugo Touvron, Matthieu Cord, and Hervé Jégou. Deit iii: Revenge of the vit, 2022. URL <https://arxiv.org/abs/2204.07118>.
- [38] Chase Walker, Sumit Jha, and Rickard Ewetz. Metric-driven attributions for vision transformers. In *International Conference on Learning Representations (ICLR)*, 2025. URL https://proceedings.iclr.cc/paper_files/paper/2025/file/4e21153e79aff242492146d78d09fcdb-Paper-Conference.pdf.
- [39] Haofan Wang, Zifan Wang, Mengnan Du, Fan Yang, Zijian Zhang, Sirui Ding, Piotr Mardziel, and Xia Hu. Score-cam: Score-weighted visual explanations for convolutional neural networks. In *Proceedings of the IEEE/CVF Conference on Computer Vision and Pattern Recognition Workshops (CVPRW)*, 2020.
- [40] Weiyan Xie, Xiao-Hui Li, Caleb Chen Cao, and Nevin L. Zhang. Vit-cx: Causal explanation of vision transformers, 2023. URL <https://arxiv.org/abs/2211.03064>.
- [41] Tingyi Yuan, Xuhong Li, Haoyi Xiong, Hui Cao, and Dejing Dou. Explaining information flow inside vision transformers using markov chain. In *NeurIPS 2021 Workshop on eXplainable AI Approaches for Debugging and Diagnosis (XAI4Debugging)*, 2021. URL <https://openreview.net/forum?id=TT-cf6QSDaQ>.
- [42] Fred Zhang and Neel Nanda. Towards best practices of activation patching in language models: Metrics and methods. In *International Conference on Learning Representations (ICLR)*, 2024. URL <https://openreview.net/forum?id=Hf17y6u9BC>.

A Broader Experiments

In this section, we present additional experimental results that further expand the empirical evaluation in the main paper. In particular, we extend the study to other model scales, including base and, where available, small variants, as well as the largest variants of the considered architectures (huge/giant models). Additional quantitative results are reported in Section A.1, and further qualitative examples are provided in Section A.2. We also provide representative insertion and deletion curves for the large variants of the backbones in Figs 8 and 9.

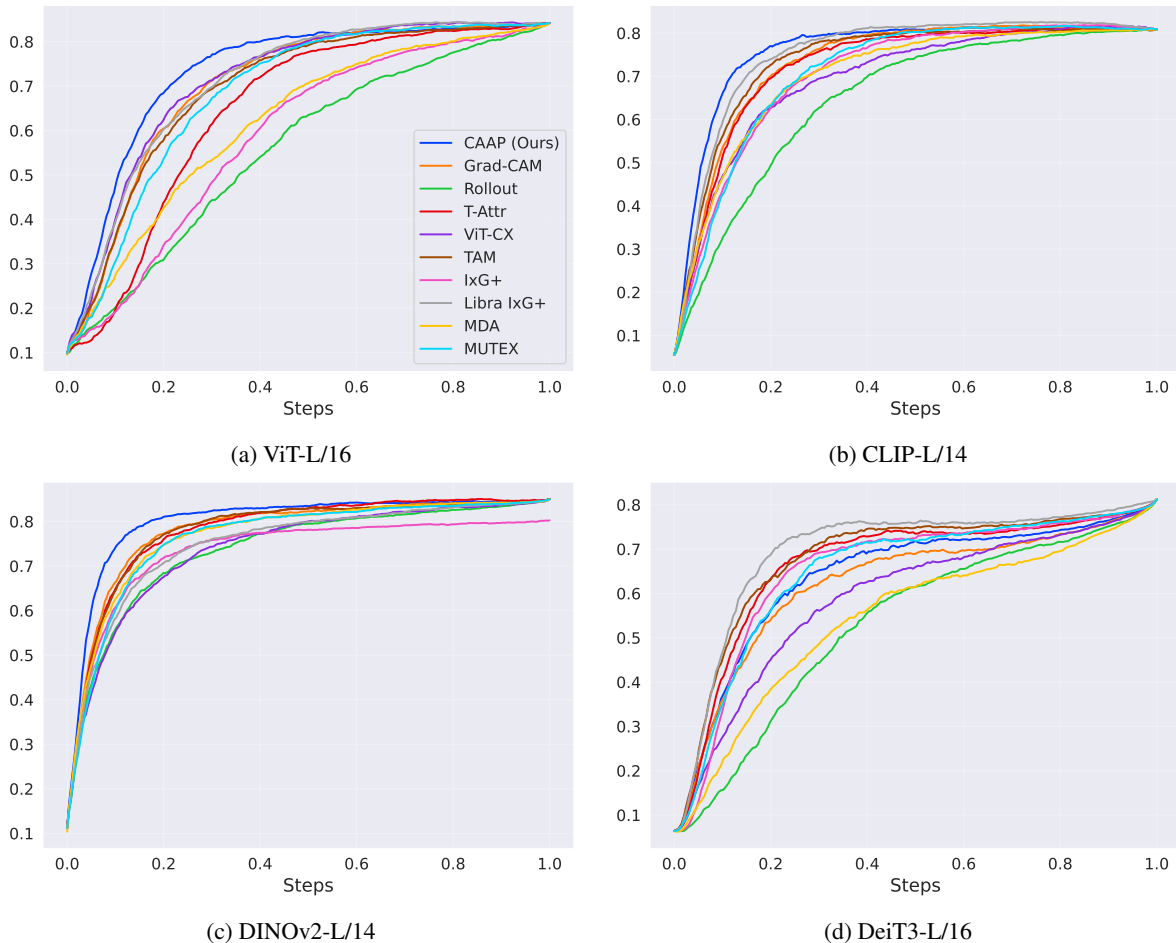


Figure 8: Representative insertion curves on ImageNet for ViT-L/16, CLIP-L/14, DINOv2-L/14, and DeiT3-L/16. Higher curves indicate that the attribution method more effectively identifies regions that positively support the model prediction.

A.1 Quantitative Results

We present broader quantitative experiments on a wider range of architecture scales. In particular, we report results for base variants in Tables 4 and 5. We also include, where available, results for small variants in Tables 6 and 7, as well as for the largest available variants in Tables 8 and 9. Across all of these settings, the trends observed in the main experiments remain consistent. Specifically, our method continues to achieve lower Deletion scores together with higher Insertion and Insertion–Deletion values than the competing baselines, indicating stronger faithfulness of the produced attributions. In addition, CAAP consistently obtains the best or among the best AUPR₁, AUPR₀, and PG results, demonstrating improved localization quality and a stronger ability to focus attribution mass on foreground object regions while suppressing background responses. This behavior is also reflected in Figure 10, which summarizes the comparison over 10 representative ViT backbones and shows that CAAP maintains the strongest overall profile across both faithfulness and localization criteria. These results further support the robustness of our approach across different architectures, training paradigms, and model scales, and suggest that our interventional patch-level attribution method generalizes well beyond the backbone configurations considered in the main paper.

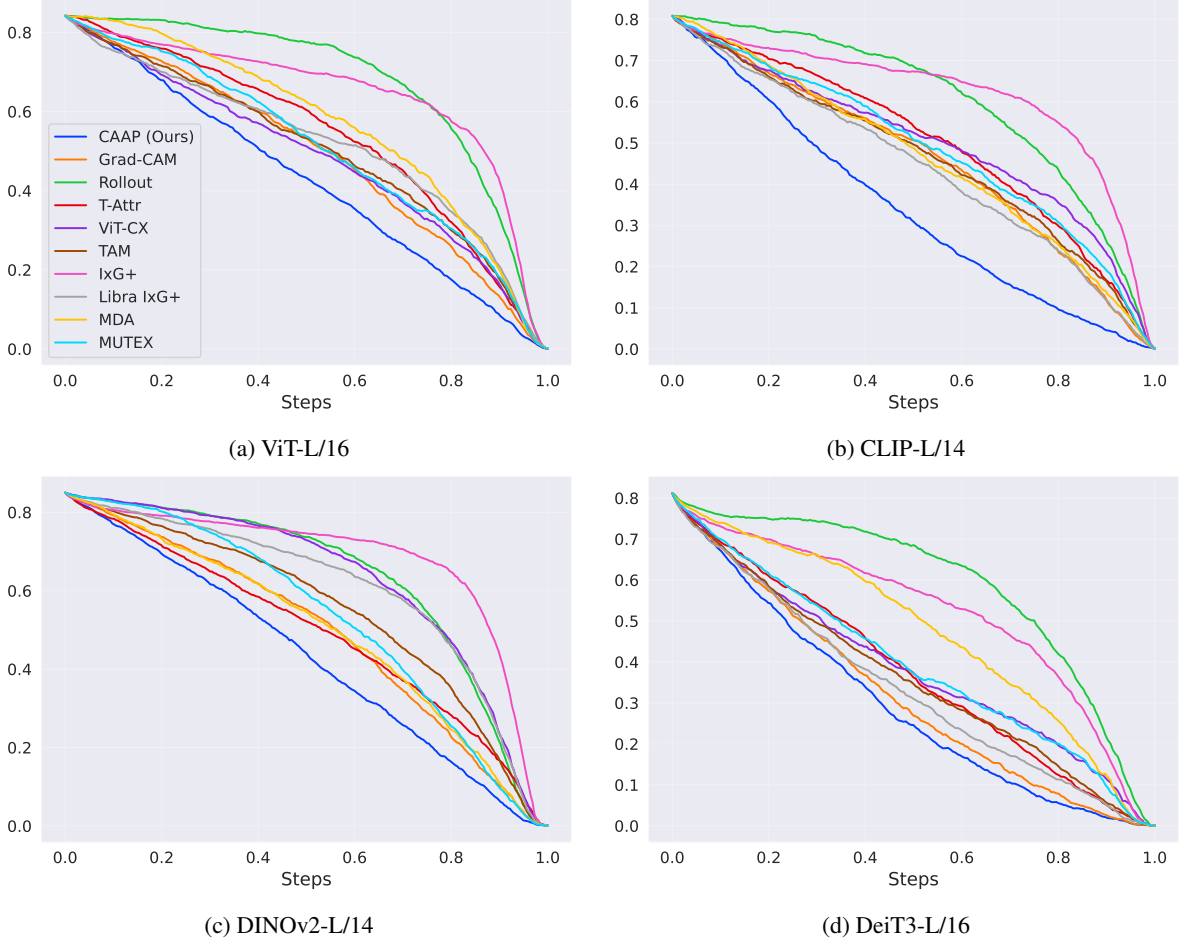


Figure 9: Representative deletion curves on ImageNet for ViT-L/16, CLIP-L/14, DINOv2-L/14, and DeiT3-L/16. Lower curves indicate that the attribution method more accurately identifies regions whose removal causes a stronger drop in model confidence.

Table 4: Faithfulness quantitative results on ImageNet for ViT-B/16 [34], Clip-B/16 [27], DINOv2-B/14 [22], and DeiT3-B/16 [37]. Deletion (\downarrow), Insertion (\uparrow), and Ins-Del (\uparrow) are reported. Best is **bold**, second best is underlined in each column.

Method	ViT-B/16 [34]			Clip-B/16 [27]			DINOv2-B/14 [22]			DeiT3-B/16 [37]		
	Del \downarrow	Ins \uparrow	Ins-Del \uparrow	Del \downarrow	Ins \uparrow	Ins-Del \uparrow	Del \downarrow	Ins \uparrow	Ins-Del \uparrow	Del \downarrow	Ins \uparrow	Ins-Del \uparrow
Grad-CAM [30]	43.92 \pm 1.41	59.07 \pm 1.25	15.15 \pm 1.40	55.21 \pm 1.21	52.68 \pm 1.04	-2.53 \pm 1.30	42.45 \pm 1.16	74.98 \pm 1.13	32.53 \pm 1.01	<u>28.96</u> \pm 0.89	61.09 \pm 0.91	32.13 \pm 0.86
Rollout [1]	54.68 \pm 1.36	49.83 \pm 1.28	-4.85 \pm 1.27	51.65 \pm 1.12	56.68 \pm 1.09	5.03 \pm 1.16	52.01 \pm 1.16	71.06 \pm 1.18	19.05 \pm 0.97	46.78 \pm 1.03	53.76 \pm 0.98	6.98 \pm 0.94
T-Attr [7]	39.49 \pm 1.32	60.73 \pm 1.25	21.24 \pm 1.26	41.73 \pm 1.10	65.18 \pm 1.04	23.45 \pm 1.09	45.09 \pm 1.10	73.29 \pm 1.19	28.20 \pm 1.02	32.61 \pm 0.96	62.75 \pm 0.98	30.13 \pm 0.93
ViT-CX [40]	<u>33.94</u> \pm 1.17	62.41 \pm 1.35	<u>28.47</u> \pm 1.43	40.78 \pm 1.21	61.78 \pm 1.06	21.00 \pm 1.44	44.25 \pm 1.23	74.66 \pm 1.13	30.41 \pm 1.15	31.64 \pm 1.00	57.73 \pm 0.95	26.10 \pm 1.10
TAM [41]	41.81 \pm 1.34	60.27 \pm 1.31	18.46 \pm 1.36	42.15 \pm 1.13	65.05 \pm 1.02	22.90 \pm 1.08	<u>41.92</u> \pm 1.15	<u>76.10</u> \pm 1.14	<u>34.17</u> \pm 1.04	29.86 \pm 0.95	<u>63.63</u> \pm 0.94	33.77 \pm 0.91
IxG+ [20]	50.41 \pm 1.53	55.90 \pm 1.37	5.49 \pm 1.37	58.07 \pm 1.21	60.46 \pm 1.11	2.39 \pm 0.96	61.41 \pm 1.28	72.55 \pm 1.21	11.14 \pm 0.77	50.43 \pm 1.16	60.96 \pm 1.07	10.53 \pm 1.00
Libra IxG+ [21]	37.53 \pm 1.34	65.41 \pm 1.28	27.88 \pm 1.33	<u>39.72</u> \pm 1.10	<u>67.34</u> \pm 0.96	<u>27.62</u> \pm 1.06	49.19 \pm 1.21	73.53 \pm 1.21	24.34 \pm 1.13	31.00 \pm 0.98	65.23 \pm 0.91	<u>34.22</u> \pm 0.90
MDA [38]	46.63 \pm 1.31	56.16 \pm 1.35	9.53 \pm 1.45	40.70 \pm 1.10	62.64 \pm 1.06	21.94 \pm 1.26	43.09 \pm 1.14	72.81 \pm 1.17	29.73 \pm 1.12	38.86 \pm 0.97	53.71 \pm 0.96	14.85 \pm 1.04
MUTEX [18]	46.36 \pm 1.40	55.79 \pm 1.27	9.43 \pm 1.35	52.71 \pm 1.31	59.31 \pm 1.01	6.60 \pm 1.22	49.76 \pm 1.05	70.30 \pm 1.24	20.54 \pm 0.90	48.91 \pm 1.23	57.11 \pm 0.93	8.20 \pm 1.14
CAAP (Ours)	32.62 \pm 1.15	<u>64.77</u> \pm 1.33	32.15 \pm 1.32	32.09 \pm 0.93	67.40 \pm 1.00	35.32 \pm 1.05	35.42 \pm 1.08	76.81 \pm 1.14	41.38 \pm 1.04	26.48 \pm 0.78	61.23 \pm 0.91	34.74 \pm 0.79

A.2 Qualitative Results

We present additional qualitative results to further illustrate the behavior of our attribution method across different object categories. As shown in Figures 11–40, our method consistently produces more precise and spatially coherent attribution maps compared to the baselines. In particular, the highlighted regions align more closely with the true object extents and exhibit sharper object boundaries, while reducing spurious activations in background regions. These examples demonstrate the robustness of our approach across diverse visual concepts, including objects with varying shapes, textures, and levels of visual complexity.

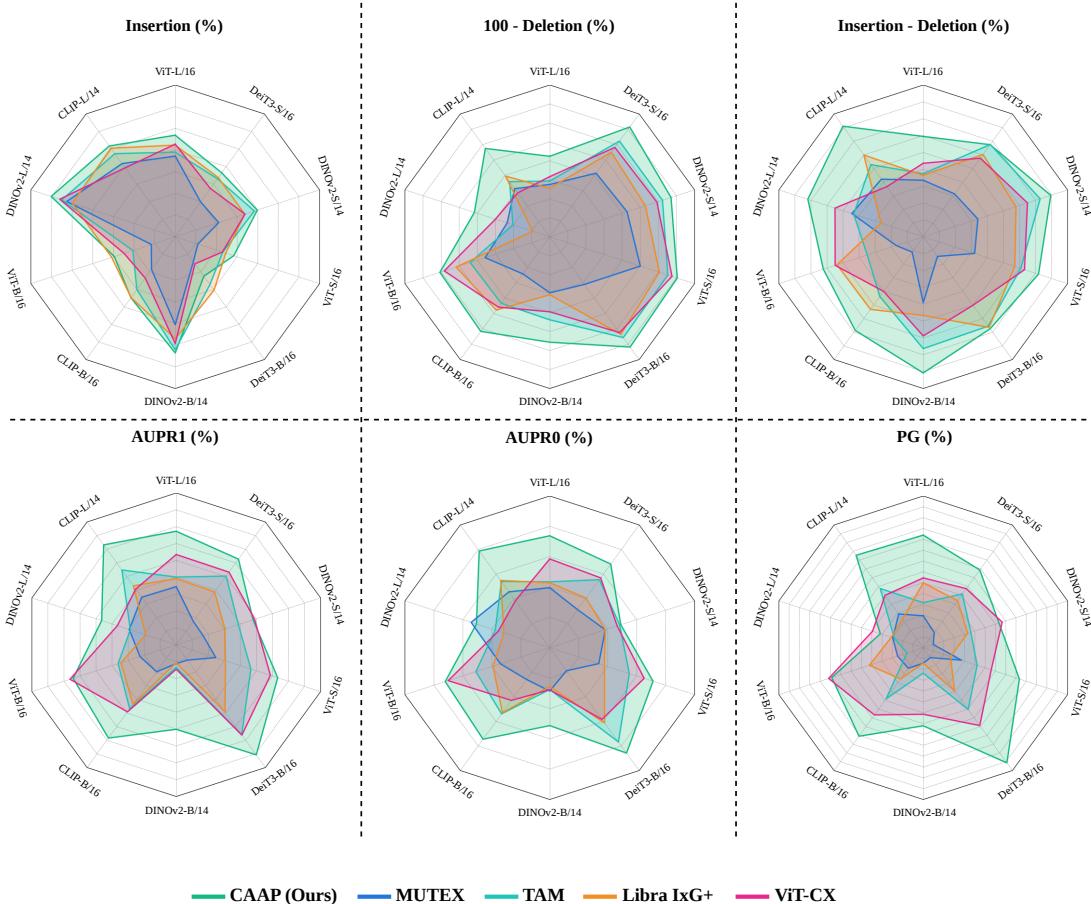


Figure 10: Radar-plot comparison of attribution performance over 10 representative ViT backbones. CAAP is compared against the four strongest baselines: MUTEX, TAM, Libra IxG+, and ViT-CX, across faithfulness and localization metrics. Higher values indicate better performance. CAAP shows the most consistently strong performance across backbones, supporting its effectiveness as a faithful and spatially precise method.

B Broader Ablation Analysis

B.1 Efficient implementation of CAAP

The efficient implementation reduces the cost of computing attention between each classification token (CLS) and the blank-context tokens. For each head, consider the self-attention update of a CLS token at layer l ,

$$z_{\text{CLS}}^{l+1} = \sum_j \frac{\exp(\langle q_{\text{CLS}}^l, k_j^l \rangle / \sqrt{d})}{\sum_m \exp(\langle q_{\text{CLS}}^l, k_m^l \rangle / \sqrt{d})} v_j^l. \quad (7)$$

In the patched context, tokens are divided into source-patched tokens $j \in \mathcal{S}(p_i)$ and blank tokens $j \notin \mathcal{S}(p_i)$. For the blank tokens we observe that the dot products $\langle q_{\text{CLS}}^{c^*}, k_{0,j}^l \rangle$ are nearly identical to those obtained in the blank context c' . Therefore we precompute two quantities for every layer and attention head.

First, we compute the normalization contribution of blank tokens,

$$Z_0^l = \sum_{j \notin \mathcal{S}(p_i)} \exp(\langle q_{\text{CLS}}^{c'}, k_{0,j}^l \rangle / \sqrt{d}), \quad (8)$$

which is reused as a fixed term in the softmax denominator. Second, we compute a prototype value vector for the blank tokens,

$$\bar{v}_0^l = \frac{1}{|\mathcal{B}|} \sum_{j \in \mathcal{B}} v_{0,j}^l, \quad (9)$$

Table 5: Localization quantitative results on ImageNet for ViT-B/16 [34], Clip-B/16 [27], DINOv2-B/14 [22], and DeiT3-B/16 [37]. AUPR₁ (↑), AUPR₀ (↑) and PG (↑) are reported. Best is **bold**, second best is underlined in each column.

Method	ViT-B/16 [34]			Clip-B/16 [27]			DINOv2-B/14 [22]			DeiT3-B/16 [37]		
	AUPR ₁ ↑	AUPR ₀ ↑	PG ↑	AUPR ₁ ↑	AUPR ₀ ↑	PG ↑	AUPR ₁ ↑	AUPR ₀ ↑	PG ↑	AUPR ₁ ↑	AUPR ₀ ↑	PG ↑
Grad-CAM [30]	46.29 _{±2.37}	73.78 _{±2.23}	45.31 _{±4.40}	34.26 _{±2.36}	66.35 _{±2.26}	22.66 _{±3.70}	37.07 _{±2.31}	72.09 _{±2.08}	46.09 _{±4.41}	66.84 _{±2.08}	86.85 _{±1.78}	66.41 _{±4.17}
Rollout [1]	31.62 _{±1.83}	65.91 _{±2.65}	14.84 _{±3.14}	39.24 _{±1.95}	68.69 _{±2.66}	28.91 _{±4.01}	33.34 _{±2.05}	67.76 _{±2.30}	36.72 _{±4.26}	32.41 _{±1.77}	67.86 _{±2.64}	11.72 _{±2.84}
T-Attr [7]	43.33 _{±1.80}	74.48 _{±2.43}	35.16 _{±4.22}	54.08 _{±1.84}	78.80 _{±2.25}	52.34 _{±4.41}	37.08 _{±2.21}	71.10 _{±2.20}	42.19 _{±4.37}	60.34 _{±1.75}	82.23 _{±1.98}	53.12 _{±4.41}
ViT-CX [40]	62.87 _{±2.13}	<u>82.34</u> _{±2.09}	67.19 _{±4.15}	<u>54.13</u> _{±2.42}	74.43 _{±2.48}	59.38 _{±4.34}	36.43 _{±2.25}	70.02 _{±2.18}	<u>51.56</u> _{±4.42}	62.86 _{±2.13}	78.92 _{±2.48}	65.62 _{±4.20}
TAM [41]	47.52 _{±1.85}	76.79 _{±2.33}	28.12 _{±3.97}	53.00 _{±2.01}	77.60 _{±2.25}	50.00 _{±4.42}	35.85 _{±2.14}	69.98 _{±2.25}	32.03 _{±4.12}	62.72 _{±1.79}	84.27 _{±1.97}	56.25 _{±4.38}
IxG+ [20]	41.26 _{±2.00}	67.79 _{±2.20}	42.19 _{±4.37}	41.49 _{±1.94}	67.07 _{±2.17}	46.88 _{±4.41}	34.15 _{±2.15}	67.99 _{±2.16}	40.62 _{±4.34}	38.27 _{±1.87}	70.59 _{±2.18}	13.28 _{±3.00}
Libra IxG+ [21]	46.63 _{±1.97}	73.36 _{±2.21}	46.88 _{±4.41}	51.27 _{±1.92}	77.33 _{±2.14}	38.28 _{±4.30}	34.45 _{±2.14}	69.43 _{±2.22}	27.34 _{±3.94}	54.16 _{±1.75}	79.75 _{±2.20}	45.31 _{±4.40}
MDA [38]	35.26 _{±1.84}	67.56 _{±2.69}	17.19 _{±3.33}	46.90 _{±2.01}	72.86 _{±2.65}	33.07 _{±4.17}	33.88 _{±2.04}	68.75 _{±2.30}	25.20 _{±3.85}	37.37 _{±1.77}	69.49 _{±2.70}	17.19 _{±3.33}
MUTEX [18]	40.56 _{±2.22}	71.89 _{±2.38}	32.81 _{±4.15}	39.13 _{±2.20}	69.50 _{±2.32}	32.03 _{±4.12}	34.73 _{±2.23}	70.28 _{±2.16}	27.34 _{±3.94}	34.76 _{±2.19}	67.43 _{±2.33}	25.78 _{±3.87}
CAAP (Ours)	<u>61.88</u> _{±2.07}	82.93 _{±1.90}	<u>65.63</u> _{±4.20}	63.96 _{±1.91}	83.60 _{±1.93}	71.88 _{±3.97}	54.63 _{±1.94}	76.88 _{±2.19}	57.03 _{±4.38}	70.26 _{±1.88}	86.88 _{±1.77}	87.50 _{±2.92}

Table 6: Faithfulness quantitative results on ImageNet for ViT-S/16 [34], DINOv2-S/14 [22], and DeiT3-S/16 [37]. Deletion (↓), Insertion (↑), and Ins–Del (↑) are reported. Best is **bold**, second best is underlined in each column.

Method	ViT-S/16 [34]			DINOv2-S/14 [22]			DeiT3-S/16 [37]		
	Del↓	Ins↑	Ins–Del↑	Del↓	Ins↑	Ins–Del↑	Del↓	Ins↑	Ins–Del↑
Grad-CAM [30]	30.70 _{±1.07}	61.41 _{±1.22}	30.71 _{±1.11}	<u>30.94</u> _{±0.99}	68.28 _{±1.15}	37.35 _{±1.02}	27.35 _{±1.04}	67.17 _{±1.32}	39.83 _{±1.17}
Rollout [1]	43.36 _{±1.16}	50.29 _{±1.26}	6.93 _{±1.15}	40.01 _{±1.09}	64.05 _{±1.20}	24.04 _{±1.05}	51.77 _{±1.33}	52.32 _{±1.29}	0.54 _{±1.12}
T-Attr [7]	30.23 _{±1.04}	60.06 _{±1.24}	29.83 _{±1.10}	34.39 _{±1.01}	66.21 _{±1.20}	31.82 _{±1.04}	33.29 _{±1.18}	65.70 _{±1.34}	32.41 _{±1.14}
ViT-CX [40]	<u>28.84</u> _{±1.01}	61.42 _{±1.27}	<u>32.58</u> _{±1.22}	33.44 _{±1.09}	66.93 _{±1.17}	33.49 _{±1.17}	33.98 _{±1.22}	63.77 _{±1.38}	29.79 _{±1.36}
TAM [41]	30.11 _{±1.06}	61.52 _{±1.26}	31.41 _{±1.13}	31.74 _{±1.04}	<u>69.20</u> _{±1.16}	<u>37.45</u> _{±1.06}	31.72 _{±1.18}	66.55 _{±1.33}	34.82 _{±1.19}
IxG+ [20]	45.73 _{±1.34}	51.75 _{±1.28}	6.01 _{±1.01}	50.67 _{±1.26}	61.95 _{±1.29}	11.28 _{±0.89}	50.63 _{±1.42}	59.43 _{±1.39}	8.81 _{±1.05}
Libra IxG+ [21]	32.70 _{±1.11}	<u>62.25</u> _{±1.26}	29.55 _{±1.19}	36.94 _{±1.13}	66.86 _{±1.22}	29.92 _{±1.20}	35.72 _{±1.31}	66.88 _{±1.35}	31.17 _{±1.18}
MDA [38]	38.09 _{±1.14}	54.93 _{±1.27}	16.84 _{±1.26}	34.53 _{±1.06}	66.46 _{±1.19}	31.93 _{±1.16}	40.97 _{±1.27}	57.86 _{±1.33}	16.89 _{±1.34}
MUTEX [18]	38.46 _{±1.19}	55.48 _{±1.22}	17.02 _{±1.07}	42.51 _{±0.98}	60.55 _{±1.24}	18.04 _{±0.93}	43.21 _{±1.34}	59.95 _{±1.28}	16.74 _{±1.10}
CAAP (Ours)	27.25 _{±0.98}	64.19 _{±1.25}	36.94 _{±1.13}	29.14 _{±0.96}	69.90 _{±1.16}	40.76 _{±1.03}	26.66 _{±1.01}	68.23 _{±0.91}	34.75 _{±0.79}

where \mathcal{B} denotes the set of blank tokens. During attribution we reuse Z_0^l and \bar{v}_0^l and compute only the terms involving the source-patched tokens dynamically. This avoids repeated evaluation of dot products and value aggregations for blank tokens across images.

This efficient implementation substantially reduces the computational complexity. In a naive implementation, each attribution requires patching operations and attention recomputation over all tokens, leading to approximately $\mathcal{O}(N^3)$ operations for an image with N tokens (N patch interventions combined with $N \times N$ attention interactions). With the proposed implementation, the attention contributions of blank tokens are precomputed and reused as a constant term ($\mathcal{O}(1)$) in the attention computation involving the CLS token and the patched tokens. As a result, only the N patch interventions are evaluated dynamically, reducing the overall computational cost to approximately $\mathcal{O}(N)$. Tables 10 and 11 compare the original CAAP implementation with the efficient version (E-CAAP). The results show that both variants produce nearly identical performance across all four ViT backbones. Faithfulness metrics (Deletion, Insertion, and Ins–Del) remain very close for all models, and the localization metrics (AUPR₁, AUPR₀, and PG) show the same pattern. These results indicate that the approximation used for the blank-token attention does not noticeably affect attribution quality while substantially reducing the computational cost.

B.2 Input-Based Intervention Baselines

To better understand the role of representation-level interventions, we compare CAAP with two simple input-based alternatives: *Simple Insertion* and *Simple Deletion*. In Simple Insertion, a selected source patch is inserted directly into a blank target image and the resulting class score is used as the attribution signal. In Simple Deletion, the selected patch is removed from the input image while all other pixels remain unchanged. These procedures operate only at the input level and do not modify internal representations across layers. All methods use the default padding (3×3 patch region). Tables 12 and 13 report the results on ImageNet across four ViT backbones.

Overall, CAAP consistently outperforms both input-based baselines. As shown in Table 12, CAAP achieves substantially lower Deletion AUC and higher Insertion AUC, leading to much larger Insertion–Deletion scores across all architectures. Localization metrics in Table 13 show the same pattern. CAAP yields higher AUPR₁, AUPR₀, and PG on most models, indicating better alignment with object regions. These results suggest that manipulating pixels alone does not reconstruct the internal evidence used by the model. In contrast, intervening

Table 7: Localization quantitative results on ImageNet for ViT-S/16 [34], DINOv2-S/14 [22], and DeiT3-S/16 [37]. AUPR₁ (↑), AUPR₀ (↑) and PG (↑) are reported. Best is **bold**, second best is underlined in each column.

Method	ViT-S/16 [34]			DINOv2-S/14 [22]			DeiT3-S/16 [37]		
	AUPR ₁ ↑	AUPR ₀ ↑	PG ↑	AUPR ₁ ↑	AUPR ₀ ↑	PG ↑	AUPR ₁ ↑	AUPR ₀ ↑	PG ↑
Grad-CAM [30]	54.18 _{±2.08}	79.60 _{±2.23}	50.00 _{±4.42}	53.34 _{±2.20}	81.38 _{±2.05}	50.78 _{±4.42}	61.08 _{±2.00}	<u>81.44</u> _{±2.09}	59.38 _{±4.34}
Rollout [1]	34.28 _{±1.91}	66.55 _{±2.67}	17.19 _{±3.33}	38.69 _{±1.86}	69.65 _{±2.54}	42.19 _{±4.37}	34.06 _{±2.00}	66.57 _{±2.48}	24.22 _{±3.79}
T-Attr [7]	44.47 _{±1.68}	76.60 _{±2.39}	18.75 _{±3.45}	49.48 _{±2.07}	76.20 _{±2.31}	43.75 _{±4.38}	55.54 _{±1.85}	75.75 _{±2.19}	<u>62.50</u> _{±4.28}
ViT-CX [40]	<u>59.01</u> _{±2.16}	<u>80.91</u> _{±2.24}	<u>53.91</u> _{±4.41}	53.98 _{±2.16}	75.50 _{±2.53}	59.38 _{±4.34}	<u>56.21</u> _{±2.16}	78.51 _{±2.28}	<u>54.69</u> _{±4.40}
TAM [41]	52.79 _{±1.83}	77.93 _{±2.25}	46.88 _{±4.41}	48.80 _{±1.89}	76.01 _{±2.36}	43.75 _{±4.38}	54.73 _{±1.88}	78.08 _{±2.17}	51.56 _{±4.42}
IxG+ [20]	38.25 _{±1.95}	65.73 _{±2.10}	48.44 _{±4.42}	38.62 _{±1.97}	66.87 _{±2.10}	43.75 _{±4.38}	37.84 _{±2.04}	67.48 _{±2.12}	42.97 _{±4.38}
Libra IxG+ [21]	44.69 _{±1.92}	72.95 _{±2.28}	33.59 _{±4.17}	44.52 _{±2.04}	73.13 _{±2.29}	42.19 _{±4.37}	48.78 _{±1.86}	73.75 _{±2.23}	47.66 _{±4.41}
MDA [38]	36.10 _{±1.85}	67.55 _{±2.72}	19.69 _{±3.53}	44.00 _{±2.04}	71.70 _{±2.74}	37.60 _{±4.33}	38.08 _{±2.07}	69.09 _{±2.62}	21.88 _{±3.65}
MUTEX [18]	41.61 _{±2.17}	71.82 _{±2.39}	39.06 _{±4.31}	37.63 _{±2.25}	73.12 _{±2.29}	25.00 _{±3.83}	37.79 _{±2.06}	71.01 _{±2.38}	28.91 _{±4.01}
CAAP (Ours)	61.34 _{±1.99}	82.69 _{±1.99}	67.97 _{±4.12}	<u>53.49</u> _{±1.94}	<u>76.23</u> _{±2.20}	<u>57.81</u> _{±4.37}	61.08 _{±2.07}	81.77 _{±2.00}	65.63 _{±4.20}

Table 8: Faithfulness quantitative results on ImageNet for CLIP-H/14 [27], DINOv2-G/14 [22], and DeiT3-H/14 [37]. Deletion (↓), Insertion (↑), and Ins–Del (†) are reported. Best is **bold**, second best is underlined in each column.

Method	CLIP-H/14 [27]			DINOv2-G/14 [22]			DeiT3-H/14 [37]		
	Del↓	Ins↑	Ins–Del†	Del↓	Ins↑	Ins–Del†	Del↓	Ins↑	Ins–Del†
Grad-CAM [30]	43.90 _{±1.63}	54.91 _{±1.28}	11.01 _{±1.64}	58.01 _{±1.86}	79.67 _{±1.67}	21.65 _{±1.54}	<u>35.53</u> _{±1.58}	64.04 _{±1.43}	28.51 _{±1.31}
Rollout [1]	44.64 _{±1.46}	54.02 _{±1.35}	9.37 _{±1.45}	69.34 _{±1.79}	76.50 _{±1.76}	7.16 _{±1.10}	63.67 _{±1.48}	52.83 _{±1.62}	-10.84 _{±1.24}
T-Attr [7]	41.07 _{±1.58}	57.55 _{±1.27}	16.48 _{±1.58}	<u>53.01</u> _{±1.99}	81.48 _{±1.55}	28.47 _{±1.64}	40.30 _{±1.70}	67.09 _{±1.45}	26.78 _{±1.51}
CausalX [40]	39.61 _{±1.67}	56.52 _{±1.34}	16.91 _{±2.00}	56.65 _{±2.07}	81.24 _{±1.55}	24.59 _{±1.74}	41.69 _{±1.82}	60.09 _{±1.51}	18.40 _{±1.80}
TAM [41]	43.26 _{±1.66}	58.45 _{±1.28}	15.19 _{±1.62}	58.32 _{±1.93}	79.47 _{±1.67}	21.15 _{±1.55}	40.66 _{±1.83}	<u>67.74</u> _{±1.43}	27.09 _{±1.54}
IxG+ [20]	50.64 _{±1.59}	54.10 _{±1.21}	3.46 _{±1.25}	69.22 _{±1.93}	80.90 _{±1.64}	11.68 _{±1.16}	59.78 _{±1.80}	65.12 _{±1.67}	5.34 _{±1.47}
Libra IxG+ [21]	37.75 _{±1.65}	<u>61.33</u> _{±1.26}	<u>23.58</u> _{±1.66}	54.09 _{±2.11}	83.32 _{±1.53}	29.23 _{±1.74}	38.23 _{±1.70}	70.67 _{±1.29}	<u>32.44</u> _{±1.53}
MDA [38]	38.62 _{±1.53}	58.08 _{±1.37}	19.47 _{±1.72}	56.50 _{±2.03}	80.94 _{±1.56}	24.44 _{±1.56}	51.85 _{±1.67}	53.08 _{±1.49}	1.24 _{±1.58}
MUTEX [18]	46.57 _{±1.62}	54.85 _{±1.31}	8.29 _{±1.54}	56.67 _{±1.81}	78.56 _{±1.67}	21.89 _{±1.42}	52.54 _{±1.93}	63.90 _{±1.50}	11.36 _{±1.67}
CAAP (Ours)	32.44 _{±1.46}	62.28 _{±1.25}	29.84 _{±1.61}	44.42 _{±1.84}	<u>82.04</u> _{±1.58}	37.62 _{±1.58}	29.55 _{±1.34}	64.49 _{±1.44}	34.94 _{±1.25}

on activations across layers preserves contextualized patch representations formed through self-attention, which leads to more faithful and spatially consistent attribution.

B.3 CNN architectures

We further evaluate the intervention strategies on convolutional architectures, including ResNet-18, ResNet-50 [14], DenseNet-161 [15], and VGG-16 [32]. The results are reported in Tables 14 and 15. Compared with the transformer results reported earlier, the overall performance of intervention-based methods is lower across both faithfulness and localization metrics. In particular, the Insertion and Insertion–Deletion scores are substantially smaller than those observed for ViT models. One possible explanation is that transformer architectures are generally more robust to distribution shifts than convolutional networks. Since intervention-based attribution methods modify the input or intermediate representations, they introduce out-of-distribution (OOD) patterns. Transformers appear to handle these perturbations more reliably, which makes intervention-based attribution more suitable for transformer-based models.

Within the CNN architectures, CAAP still achieves the best overall results in most cases. As shown in Table 14, CAAP produces the highest Insertion–Deletion scores across all four models and often improves the Insertion score, while maintaining competitive Deletion AUC. Localization metrics in Table 15 show the same trend, where CAAP consistently achieves the highest AUPR₁ and AUPR₀ and improves PG in most cases. Another difference from the transformer experiments is that the Simple Deletion baseline generally outperforms Simple Insertion on CNNs. This behavior suggests that removing pixels may better reflect the model’s reliance on local features in convolutional networks. In contrast, inserting isolated patches into a blank image provides limited evidence for the classifier, possibly due to the OOD nature of the input.

Table 9: Localization quantitative results on ImageNet for CLIP-H/14 [27], DINOv2-G/14 [22], and DeiT3-H/14 [37]. AUPR₁ (↑), AUPR₀ (↑), and PG (↑) are reported. Best is **bold**, second best is underlined in each column.

Method	CLIP-H/14 [27]			DINOv2-G/14 [22]			DeiT3-H/14 [37]		
	AUPR ₁ ↑	AUPR ₀ ↑	PG ↑	AUPR ₁ ↑	AUPR ₀ ↑	PG ↑	AUPR ₁ ↑	AUPR ₀ ↑	PG ↑
Grad-CAM [30]	39.31 _{±2.24}	71.89 _{±2.32}	27.34 _{±3.94}	47.64 _{±2.25}	<u>77.12</u> _{±2.20}	44.53 _{±4.39}	64.60 _{±1.88}	85.08 _{±1.89}	<u>62.50</u> _{±4.28}
Rollout [1]	41.40 _{±2.15}	71.28 _{±2.54}	37.50 _{±4.28}	33.66 _{±1.97}	65.90 _{±2.38}	38.28 _{±4.30}	28.49 _{±1.95}	64.97 _{±2.34}	2.34 _{±1.34}
T-Attr [7]	43.87 _{±1.76}	73.82 _{±2.44}	33.59 _{±4.17}	<u>52.91</u> _{±1.79}	76.06 _{±2.46}	<u>46.88</u> _{±4.41}	54.06 _{±1.63}	80.76 _{±2.06}	28.91 _{±4.01}
CausalX [40]	51.98 _{±2.32}	75.55 _{±2.35}	<u>58.59</u> _{±4.35}	45.94 _{±2.37}	71.65 _{±2.38}	41.41 _{±4.35}	52.49 _{±2.40}	76.23 _{±2.26}	50.78 _{±4.42}
TAM [41]	46.87 _{±1.91}	73.12 _{±2.47}	42.19 _{±4.37}	40.35 _{±1.87}	71.75 _{±2.53}	28.12 _{±3.97}	59.52 _{±1.79}	80.91 _{±2.09}	53.91 _{±4.41}
IxG+ [20]	32.55 _{±2.13}	68.64 _{±2.10}	22.66 _{±3.70}	39.26 _{±1.97}	67.08 _{±2.12}	39.06 _{±4.31}	34.94 _{±1.89}	69.09 _{±2.18}	8.59 _{±2.48}
Libra IxG+ [21]	<u>57.57</u> _{±1.82}	<u>78.46</u> _{±2.09}	57.03 _{±4.38}	46.72 _{±1.80}	73.03 _{±2.33}	47.66 _{±4.41}	52.22 _{±1.72}	79.70 _{±2.03}	2.34 _{±1.34}
MDA [38]	48.22 _{±3.25}	70.00 _{±4.03}	30.77 _{±6.40}	40.89 _{±2.92}	64.86 _{±4.08}	13.21 _{±4.65}	31.18 _{±2.00}	66.16 _{±2.57}	14.17 _{±3.09}
MUTEX [18]	39.40 _{±2.24}	69.56 _{±2.29}	39.84 _{±4.33}	43.24 _{±2.17}	77.42 _{±2.18}	35.16 _{±4.22}	38.87 _{±2.06}	69.99 _{±2.44}	19.53 _{±3.50}
CAAP (Ours)	63.05 _{±1.83}	81.30 _{±2.00}	65.63 _{±4.20}	56.22 _{±3.01}	77.03 _{±3.29}	50.91 _{±6.74}	68.70 _{±1.87}	86.24 _{±1.83}	72.66 _{±3.94}

Table 10: Faithfulness quantitative results for CAAP and Efficient-CAAP (E-CAAP) on ImageNet. Deletion (↓), Insertion (↑), and Ins-Del (↑) are reported.

Method	ViT-L/16 [34]			CLIP-L/14 [27]			DINOv2-L/14 [22]			DeiT3-L/16 [37]		
	Del↓	Ins↑	Ins-Del↑									
CAAP	43.61 _{±2.73}	71.10 _{±2.61}	27.50 _{±2.71}	34.20 _{±2.21}	74.92 _{±2.01}	40.73 _{±2.15}	43.48 _{±2.76}	79.05 _{±2.50}	35.57 _{±2.16}	28.93 _{±1.84}	65.79 _{±2.06}	36.86 _{±1.82}
E-CAAP	42.56 _{±2.80}	70.23 _{±2.56}	27.67 _{±2.63}	33.56 _{±2.42}	74.68 _{±2.58}	41.12 _{±2.39}	41.73 _{±2.79}	78.44 _{±2.75}	36.71 _{±2.65}	29.72 _{±1.87}	65.55 _{±2.33}	35.83 _{±1.97}

Table 11: Localization quantitative results for CAAP and Efficient-CAAP (E-CAAP) on ImageNet. AUPR₁ (↑), AUPR₀ (↑), and PG (↑) are reported.

Method	ViT-L/16 [34]			CLIP-L/14 [27]			DINOv2-L/14 [22]			DeiT3-L/16 [37]		
	AUPR ₁ ↑	AUPR ₀ ↑	PG ↑	AUPR ₁ ↑	AUPR ₀ ↑	PG ↑	AUPR ₁ ↑	AUPR ₀ ↑	PG ↑	AUPR ₁ ↑	AUPR ₀ ↑	PG ↑
CAAP	62.29 _{±3.70}	80.83 _{±3.75}	77.78 _{±8.00}	64.30 _{±3.68}	84.44 _{±3.29}	74.07 _{±8.43}	53.04 _{±3.88}	74.96 _{±4.52}	37.04 _{±9.29}	73.53 _{±3.10}	87.19 _{±3.17}	85.19 _{±6.84}
E-CAAP	61.17 _{±3.11}	80.28 _{±3.23}	75.66 _{±4.71}	66.59 _{±2.41}	83.35 _{±3.11}	73.14 _{±4.99}	54.45 _{±3.16}	75.99 _{±3.14}	38.75 _{±4.96}	72.41 _{±2.84}	86.28 _{±2.23}	87.67 _{±3.16}

Table 12: Faithfulness quantitative results for Simple Insertion, Simple Deletion, and CAAP on ImageNet. Deletion (↓), Insertion (↑), and Ins-Del (↑) are reported. Best is **bold**, second best is underlined in each column.

Method	ViT-L/16 [34]			CLIP-L/14 [27]			DINOv2-L/14 [22]			DeiT3-L/16 [37]		
	Del↓	Ins↑	Ins-Del↑									
Simple Insertion	<u>55.63</u> _{±1.24}	69.51 _{±1.19}	10.63 _{±1.01}	43.86 _{±1.10}	<u>75.33</u> _{±0.87}	14.93 _{±0.83}	<u>49.79</u> _{±1.20}	79.41 _{±1.11}	19.59 _{±0.79}	<u>33.33</u> _{±0.92}	<u>64.50</u> _{±0.97}	<u>22.16</u> _{±0.75}
Simple Deletion	58.89 _{±1.37}	<u>69.75</u> _{±1.07}	<u>10.86</u> _{±1.20}	60.40 _{±1.27}	72.38 _{±0.89}	11.98 _{±1.14}	59.82 _{±1.33}	80.18 _{±1.05}	<u>20.36</u> _{±0.93}	42.34 _{±0.90}	61.13 _{±0.89}	18.79 _{±0.88}
CAAP (Ours)	42.67 _{±1.16}	73.42 _{±1.07}	30.75 _{±1.18}	34.35 _{±0.99}	75.88 _{±0.85}	41.52 _{±1.02}	43.11 _{±1.14}	<u>80.09</u> _{±1.08}	36.98 _{±1.00}	31.56 _{±0.91}	64.84 _{±0.93}	33.28 _{±0.85}

Table 13: Localization quantitative results for Simple Insertion, Simple Deletion, and CAAP on ImageNet. AUPR₁ (↑), AUPR₀ (↑) and PG (↑) are reported. Best is **bold**, second best is underlined in each column.

Method	ViT-L/16 [34]			CLIP-L/14 [27]			DINOv2-L/14 [22]			DeiT3-L/16 [37]		
	AUPR ₁ ↑	AUPR ₀ ↑	PG ↑	AUPR ₁ ↑	AUPR ₀ ↑	PG ↑	AUPR ₁ ↑	AUPR ₀ ↑	PG ↑	AUPR ₁ ↑	AUPR ₀ ↑	PG ↑
Simple Insertion	<u>49.28</u> _{±1.99}	<u>71.10</u> _{±2.18}	<u>61.72</u> _{±4.30}	<u>55.32</u> _{±1.96}	<u>75.55</u> _{±2.09}	<u>59.38</u> _{±4.34}	<u>48.13</u> _{±2.02}	<u>72.81</u> _{±2.16}	52.34 _{±4.41}	<u>55.59</u> _{±1.97}	79.02 _{±1.99}	<u>62.50</u> _{±4.28}
Simple Deletion	40.82 _{±2.07}	67.53 _{±2.23}	46.09 _{±4.41}	40.44 _{±2.10}	66.01 _{±2.18}	58.59 _{±4.35}	39.05 _{±2.09}	67.45 _{±2.27}	<u>45.31</u> _{±4.40}	47.51 _{±2.50}	<u>80.74</u> _{±1.69}	57.81 _{±4.37}
CAAP (Ours)	63.40 _{±2.01}	83.40 _{±1.99}	73.44 _{±3.90}	66.42 _{±1.78}	84.86 _{±1.89}	74.22 _{±3.87}	52.76 _{±1.86}	76.68 _{±2.17}	41.41 _{±4.35}	71.21 _{±1.86}	86.93 _{±1.85}	82.81 _{±3.30}

Table 14: Faithfulness quantitative results for Simple Insertion, Simple Deletion, and CAAP on ResNet-18, ResNet-50, DenseNet-161, and VGG-16. Deletion (↓), Insertion (↑), and Ins-Del (↑) are reported. Best is **bold**, second best is underlined in each column.

Method	ResNet-18 [14]			ResNet-50 [14]			DenseNet-161 [15]			VGG-16 [32]		
	Del↓	Ins↑	Ins-Del↑									
Simple Insertion	16.05 _{±0.67}	38.75 _{±1.20}	22.70 _{±1.13}	15.65 _{±0.64}	49.11 _{±1.28}	33.46 _{±1.25}	20.83 _{±0.78}	52.87 _{±1.34}	32.04 _{±1.26}	14.60 _{±0.62}	41.01 _{±1.22}	26.41 _{±1.14}
Simple Deletion	<u>12.54</u> _{±0.57}	<u>54.44</u> _{±1.19}	<u>41.90</u> _{±1.09}	<u>14.74</u> _{±0.78}	<u>62.19</u> _{±1.18}	<u>47.45</u> _{±1.22}	<u>20.35</u> _{±0.95}	<u>65.98</u> _{±1.16}	<u>45.64</u> _{±1.17}	<u>11.66</u> _{±0.60}	<u>57.54</u> _{±1.17}	<u>45.88</u> _{±1.09}
CAAP (Ours)	13.53 _{±0.58}	55.64 _{±1.19}	42.11 _{±1.04}	15.61 _{±0.66}	64.85 _{±1.14}	49.24 _{±1.00}	20.33 _{±0.77}	67.43 _{±1.12}	47.10 _{±0.97}	9.53 _{±0.44}	57.62 _{±1.21}	48.08 _{±1.08}

Table 15: Localization quantitative results for Simple Insertion, Simple Deletion, and CAAP on ResNet-18, ResNet-50, DenseNet-161, and VGG-16. $AUPR_1$ (\uparrow), $AUPR_0$ (\uparrow), and PG (\uparrow) are reported. Best is **bold**, second best is underlined in each column.

Method	ResNet-18 [14]			ResNet-50 [14]			DenseNet-161 [15]			VGG-16 [32]		
	$AUPR_1$ \uparrow	$AUPR_0$ \uparrow	PG \uparrow	$AUPR_1$ \uparrow	$AUPR_0$ \uparrow	PG \uparrow	$AUPR_1$ \uparrow	$AUPR_0$ \uparrow	PG \uparrow	$AUPR_1$ \uparrow	$AUPR_0$ \uparrow	PG \uparrow
Simple Insertion	36.91 \pm 2.23	65.50 \pm 2.37	47.66 \pm 4.41	42.00 \pm 2.21	69.03 \pm 2.28	56.25 \pm 4.38	39.70 \pm 2.24	67.83 \pm 2.19	49.22 \pm 4.42	35.12 \pm 2.15	64.95 \pm 2.31	42.19 \pm 4.37
Simple Deletion	50.49 \pm 2.20	72.09 \pm 2.31	60.94 \pm 4.31	49.40 \pm 2.08	69.96 \pm 2.35	64.06 \pm 4.24	49.54 \pm 2.14	71.87 \pm 2.25	62.50 \pm 4.28	51.61 \pm 2.23	73.62 \pm 2.32	64.84 \pm 4.22
CAAP (Ours)	61.10 \pm 2.18	84.68 \pm 1.80	69.53 \pm 4.07	59.32 \pm 2.07	84.55 \pm 1.82	64.84 \pm 4.22	62.85 \pm 2.22	84.72 \pm 1.85	75.78 \pm 3.79	55.82 \pm 2.07	79.39 \pm 2.10	62.50 \pm 4.28

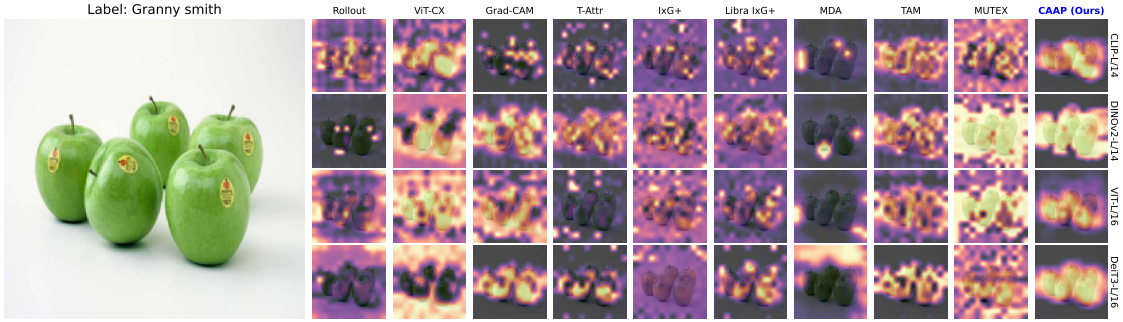


Figure 11: Visualization of attribution maps produced by different methods across various models. The target object is an Granny smith, and our method more accurately delineates the object boundaries compared to the baselines.

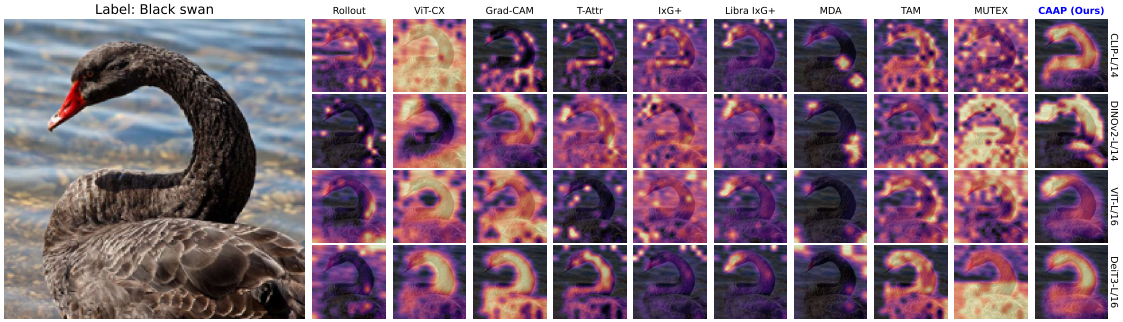


Figure 12: Visualization of attribution maps produced by different methods across various models. The target object is an Black swan, and our method more accurately delineates the object boundaries compared to the baselines.

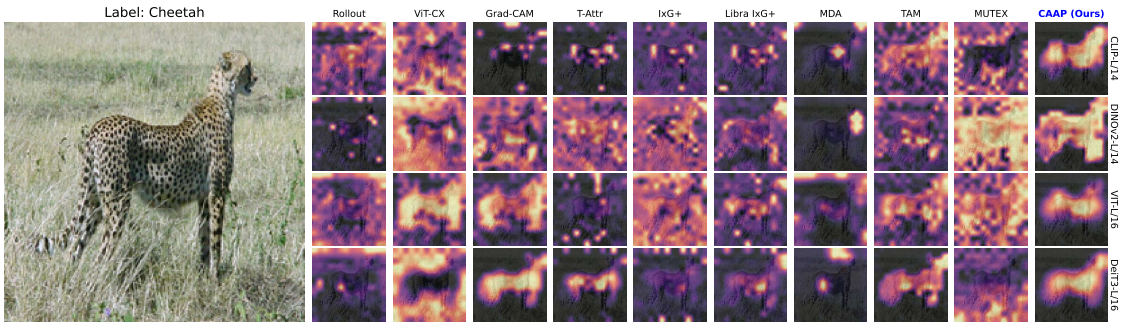


Figure 13: Visualization of attribution maps produced by different methods across various models. The target object is an Cheetah, and our method more accurately delineates the object boundaries compared to the baselines.

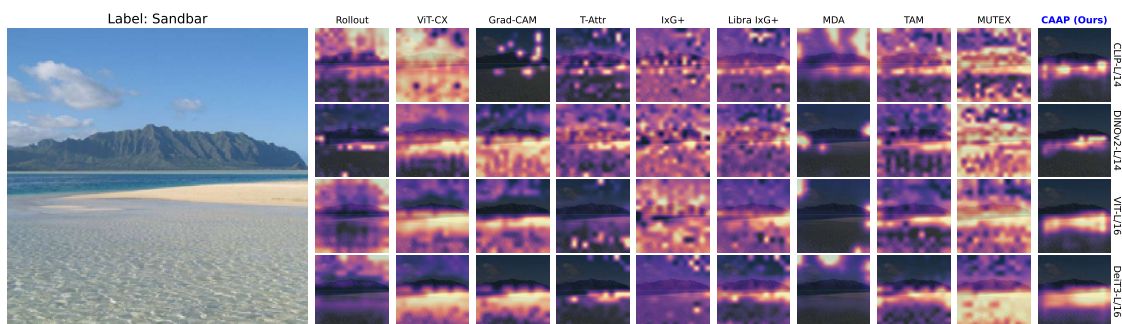


Figure 14: Visualization of attribution maps produced by different methods across various models. The target object is a Sandbar, and our method more accurately delineates the object boundaries compared to the baselines.

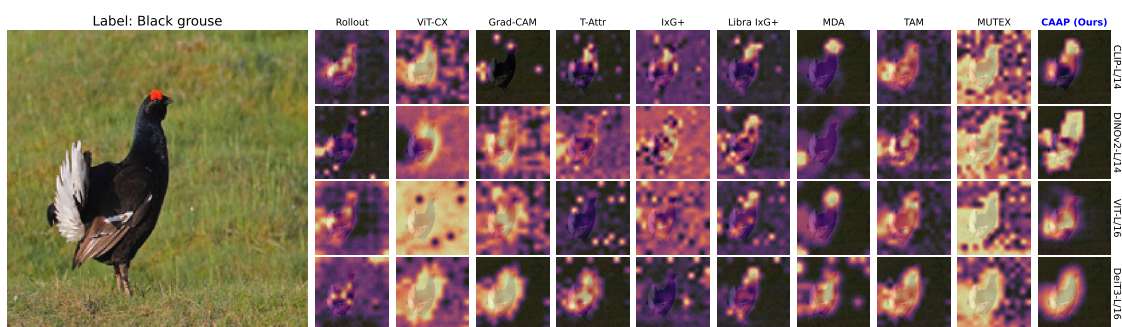


Figure 15: Visualization of attribution maps produced by different methods across various models. The target object is a Black grouse, and our method more accurately delineates the object boundaries compared to the baselines.

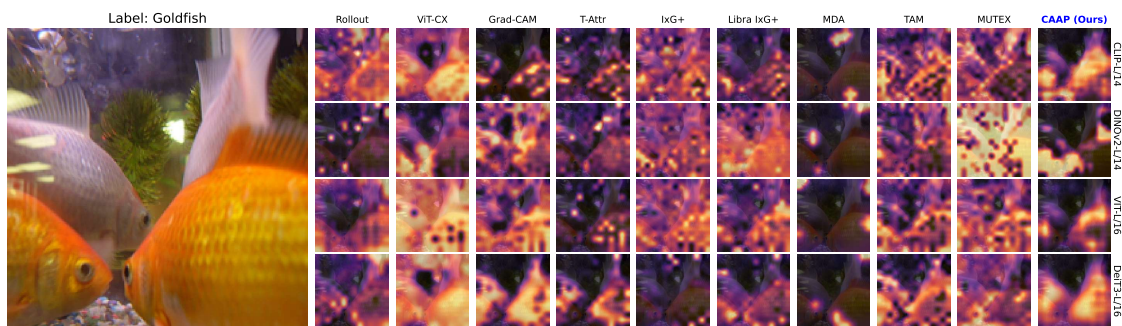


Figure 16: Visualization of attribution maps produced by different methods across various models. The target object is a Goldfish, and our method more accurately delineates the object boundaries compared to the baselines.

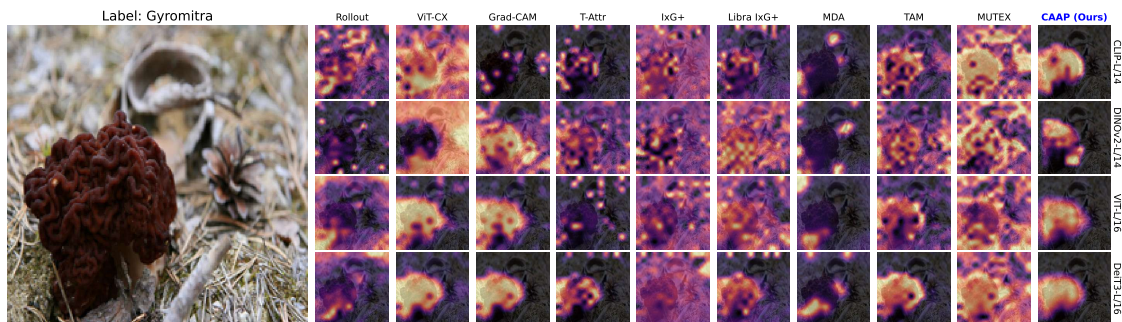


Figure 17: Visualization of attribution maps produced by different methods across various models. The target object is a Gyromitra, and our method more accurately delineates the object boundaries compared to the baselines.

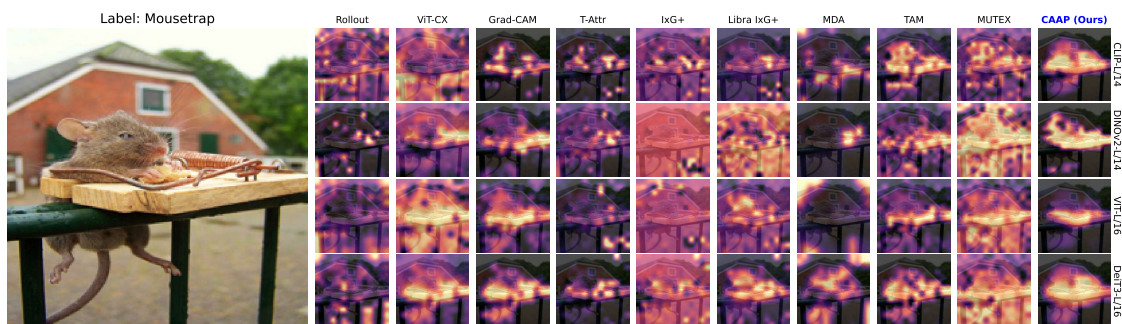


Figure 18: Visualization of attribution maps produced by different methods across various models. The target object is a Mousetrap, and our method more accurately delineates the object boundaries compared to the baselines.

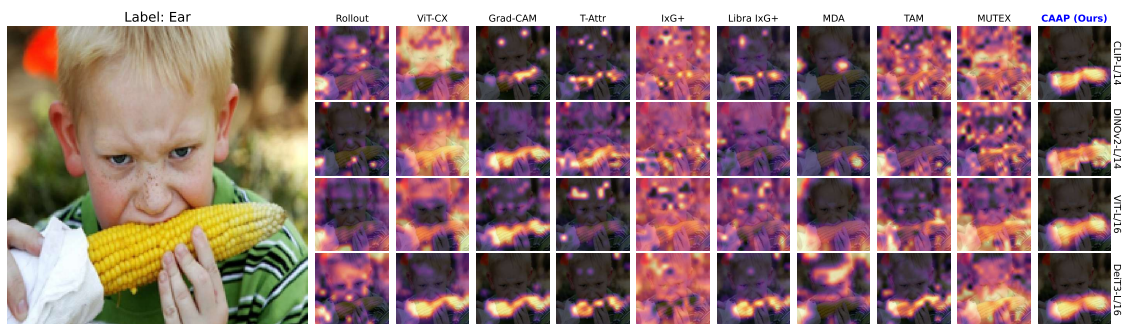


Figure 19: Visualization of attribution maps produced by different methods across various models. The target object is an Ear, and our method more accurately delineates the object boundaries compared to the baselines.

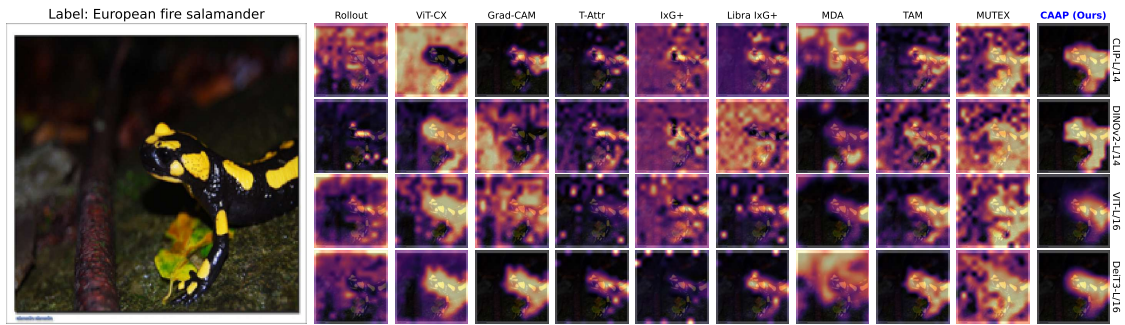


Figure 20: Visualization of attribution maps produced by different methods across various models. The target object is a European fire salamander, and our method more accurately delineates the object boundaries compared to the baselines.

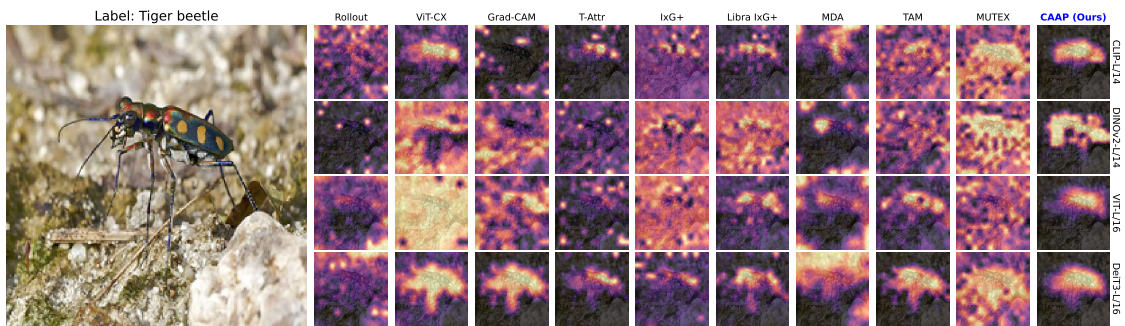


Figure 21: Visualization of attribution maps produced by different methods across various models. The target object is a Tiger beetle, and our method more accurately delineates the object boundaries compared to the baselines.

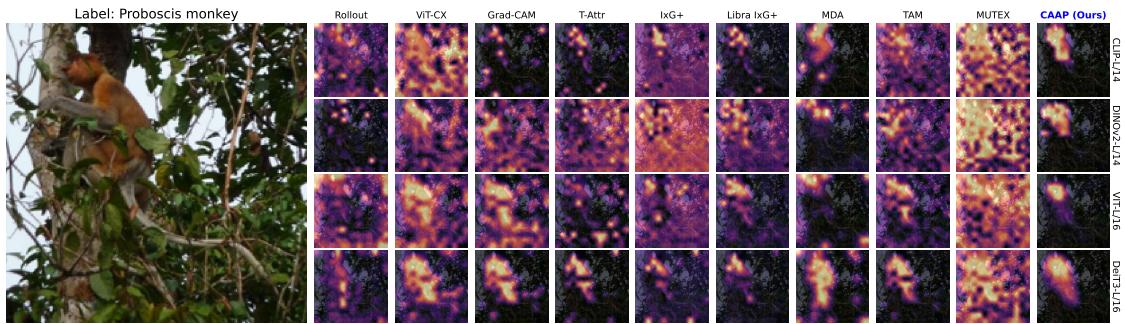


Figure 22: Visualization of attribution maps produced by different methods across various models. The target object is a Proboscis monkey, and our method more accurately delineates the object boundaries compared to the baselines.

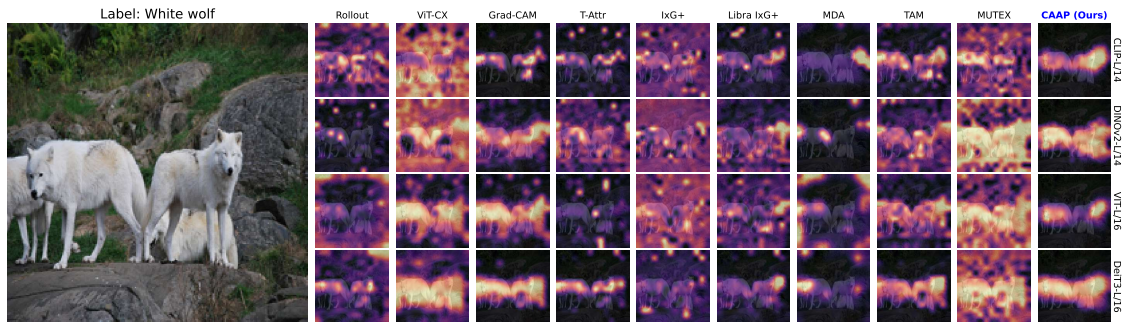


Figure 23: Visualization of attribution maps produced by different methods across various models. The target object is a White wolf, and our method more accurately delineates the object boundaries compared to the baselines.

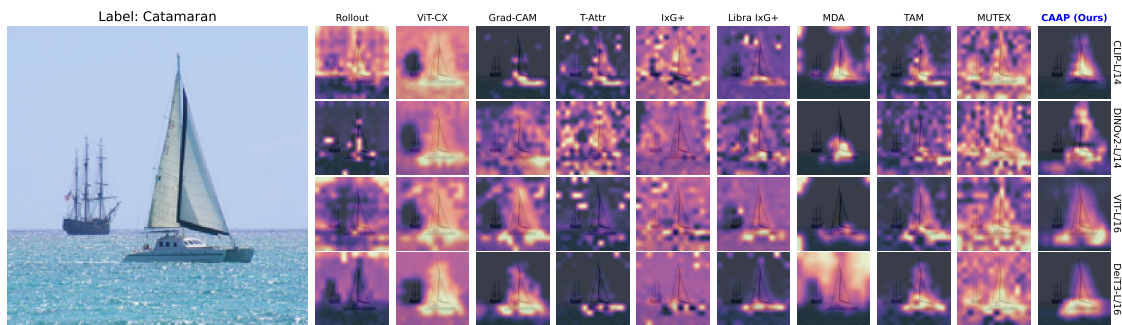


Figure 24: Visualization of attribution maps produced by different methods across various models. The target object is a Catamaran, and our method more accurately delineates the object boundaries compared to the baselines.

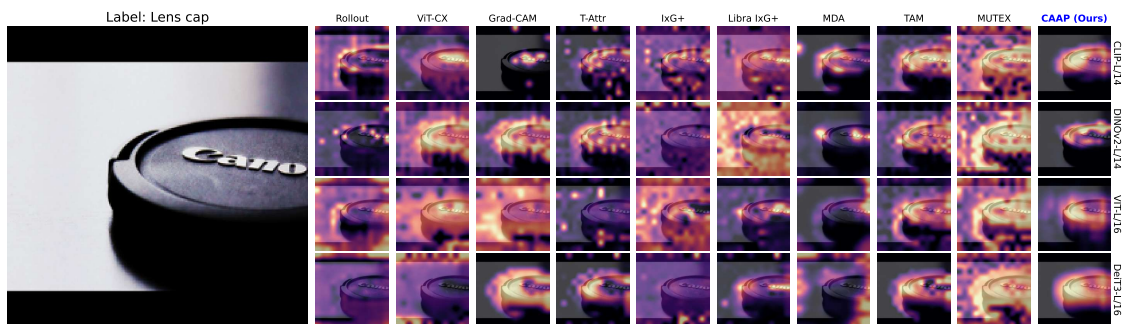


Figure 25: Visualization of attribution maps produced by different methods across various models. The target object is a Lens cap, and our method more accurately delineates the object boundaries compared to the baselines.

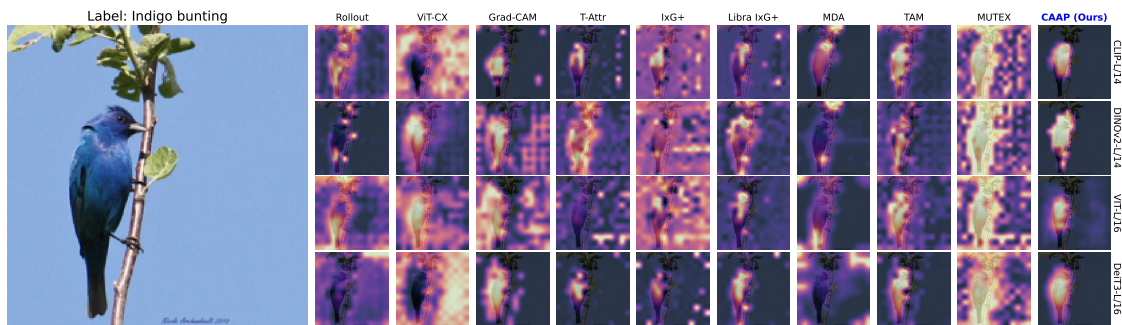


Figure 26: Visualization of attribution maps produced by different methods across various models. The target object is an Indigo bunting, and our method more accurately delineates the object boundaries compared to the baselines.

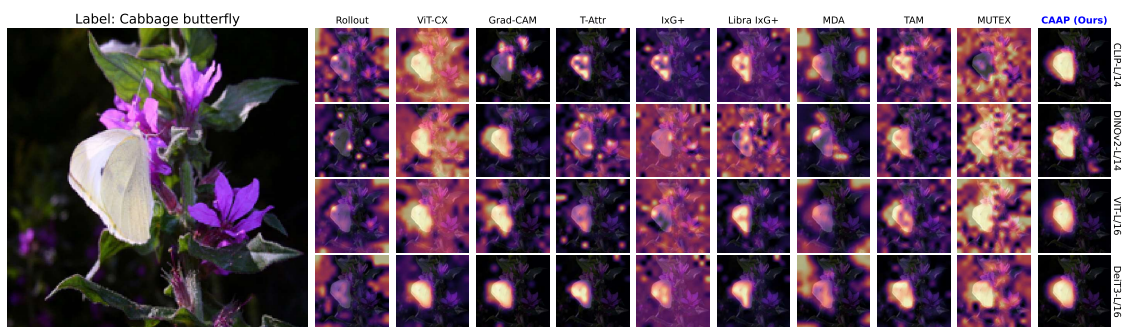


Figure 27: Visualization of attribution maps produced by different methods across various models. The target object is a Cabbage butterfly, and our method more accurately delineates the object boundaries compared to the baselines.

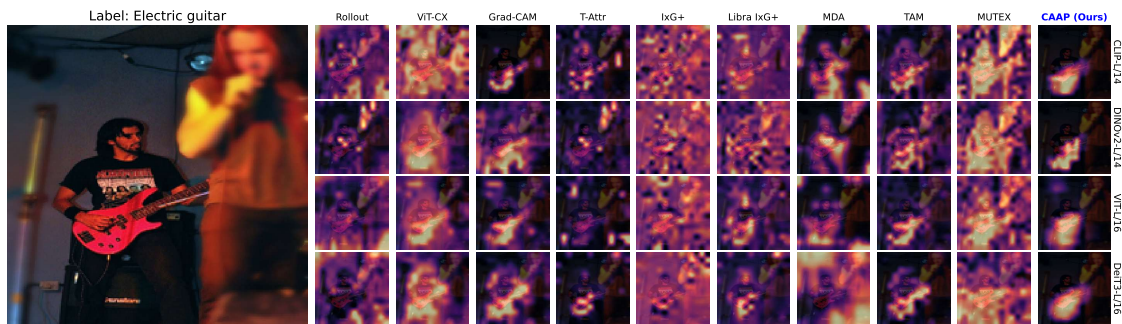


Figure 28: Visualization of attribution maps produced by different methods across various models. The target object is an Electric guitar, and our method more accurately delineates the object boundaries compared to the baselines.

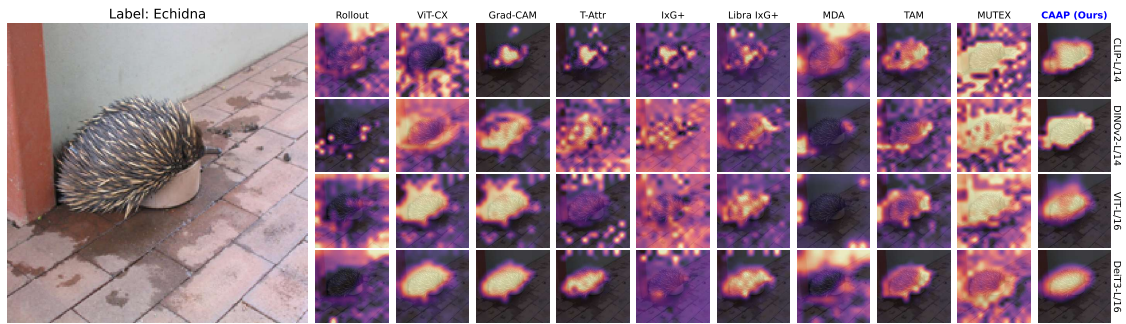


Figure 29: Visualization of attribution maps produced by different methods across various models. The target object is an Echidna, and our method more accurately delineates the object boundaries compared to the baselines.

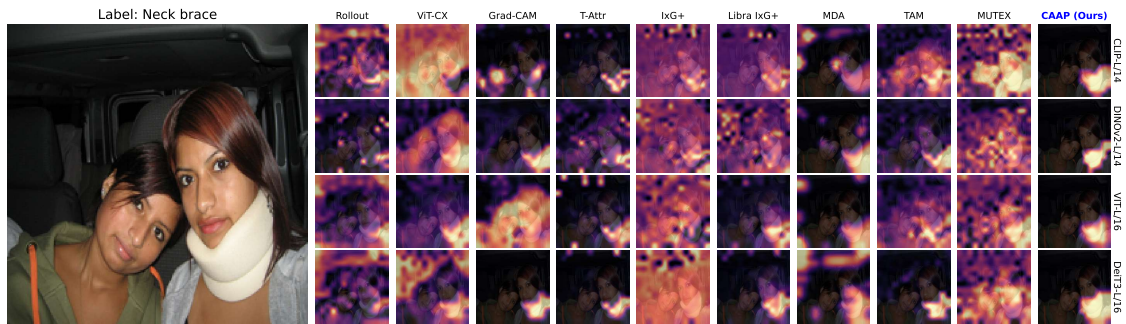


Figure 30: Visualization of attribution maps produced by different methods across various models. The target object is a Neck brace, and our method more accurately delineates the object boundaries compared to the baselines.

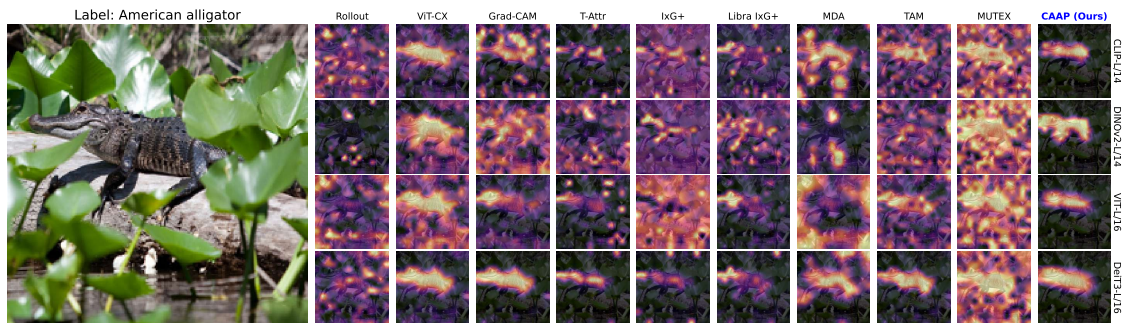


Figure 31: Visualization of attribution maps produced by different methods across various models. The target object is an American alligator, and our method more accurately delineates the object boundaries compared to the baselines.

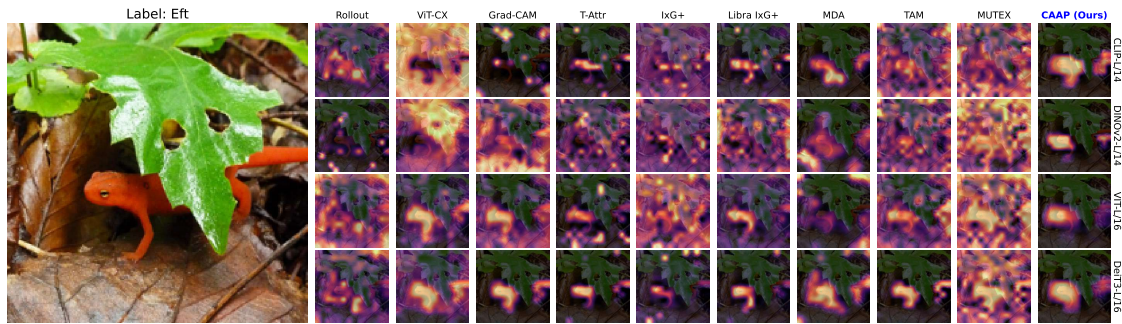


Figure 32: Visualization of attribution maps produced by different methods across various models. The target object is an Eft, and our method more accurately delineates the object boundaries compared to the baselines.

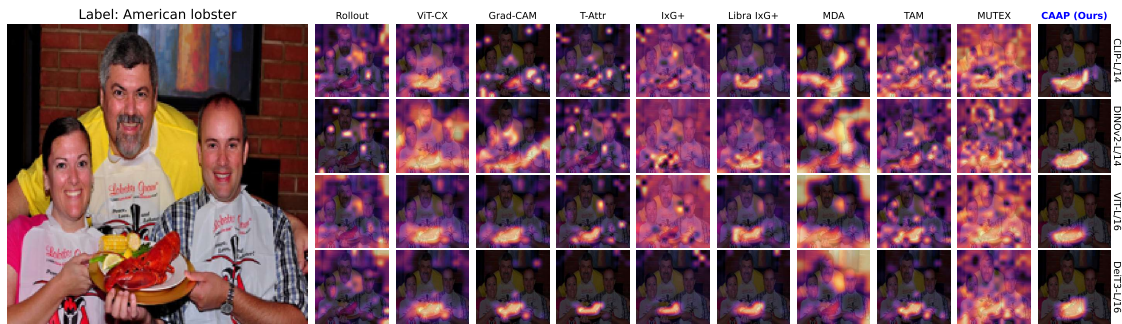


Figure 33: Visualization of attribution maps produced by different methods across various models. The target object is an American lobster, and our method more accurately delineates the object boundaries compared to the baselines.

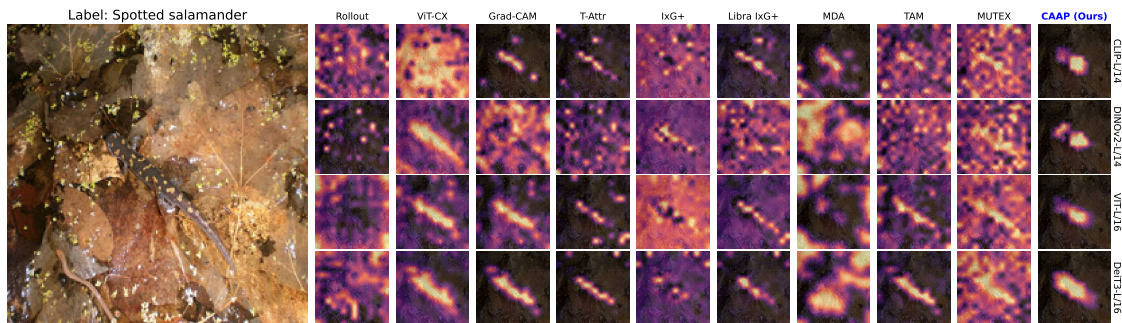


Figure 34: Visualization of attribution maps produced by different methods across various models. The target object is a Spotted salamander, and our method more accurately delineates the object boundaries compared to the baselines.

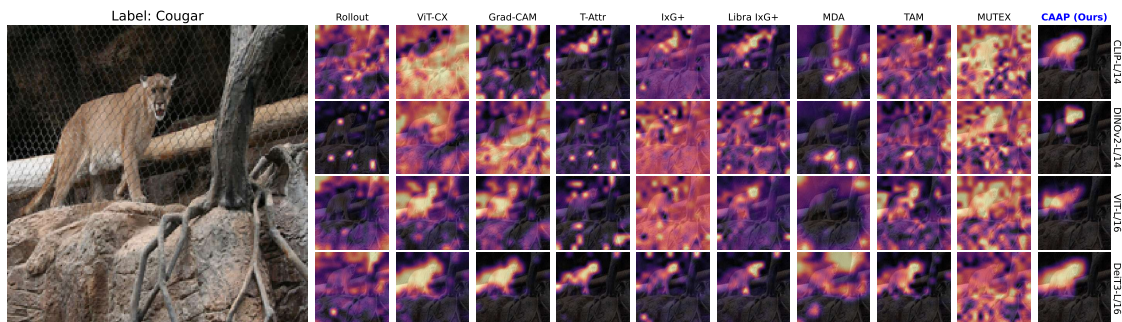


Figure 35: Visualization of attribution maps produced by different methods across various models. The target object is a Cougar, and our method more accurately delineates the object boundaries compared to the baselines.

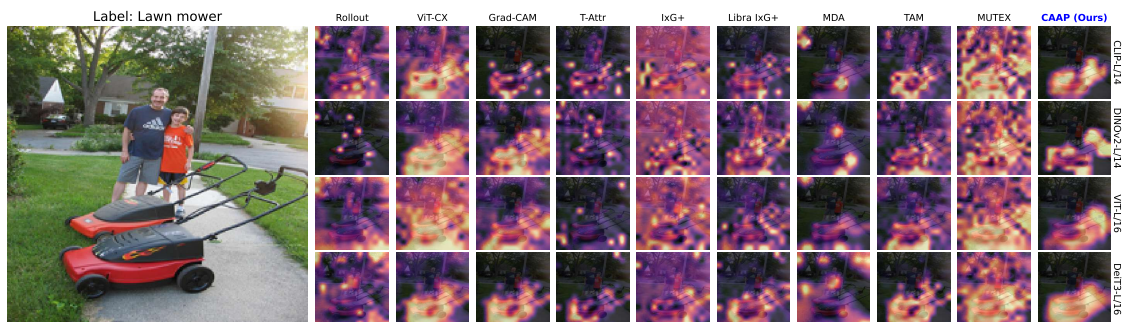


Figure 36: Visualization of attribution maps produced by different methods across various models. The target object is a Lawn mower, and our method more accurately delineates the object boundaries compared to the baselines.

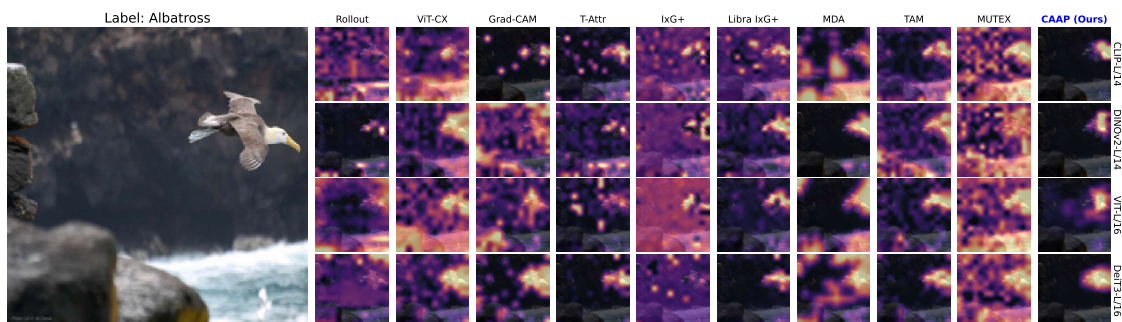


Figure 37: Visualization of attribution maps produced by different methods across various models. The target object is an Albatross, and our method more accurately delineates the object boundaries compared to the baselines.

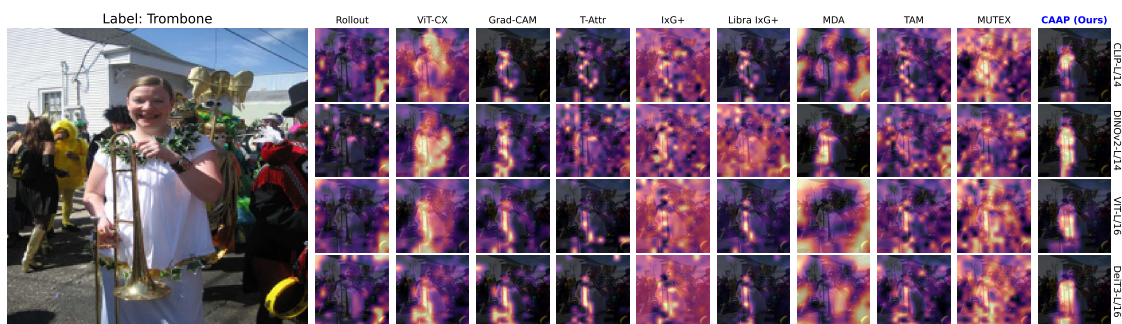


Figure 38: Visualization of attribution maps produced by different methods across various models. The target object is a Trombone, and our method more accurately delineates the object boundaries compared to the baselines.

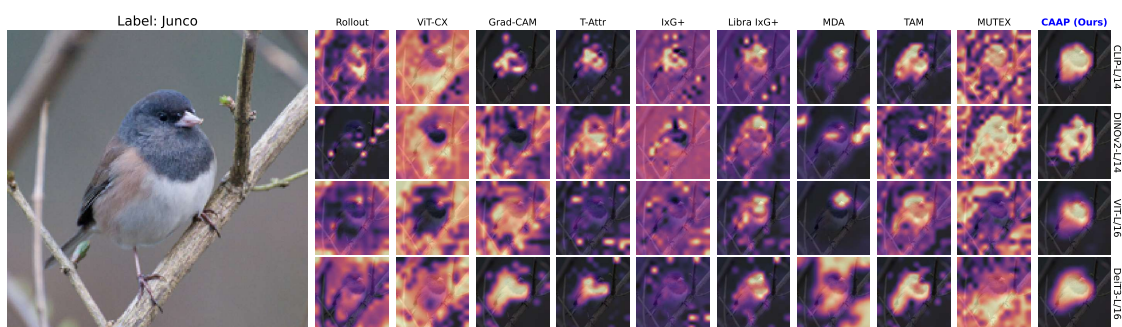


Figure 39: Visualization of attribution maps produced by different methods across various models. The target object is a Junco, and our method more accurately delineates the object boundaries compared to the baselines.

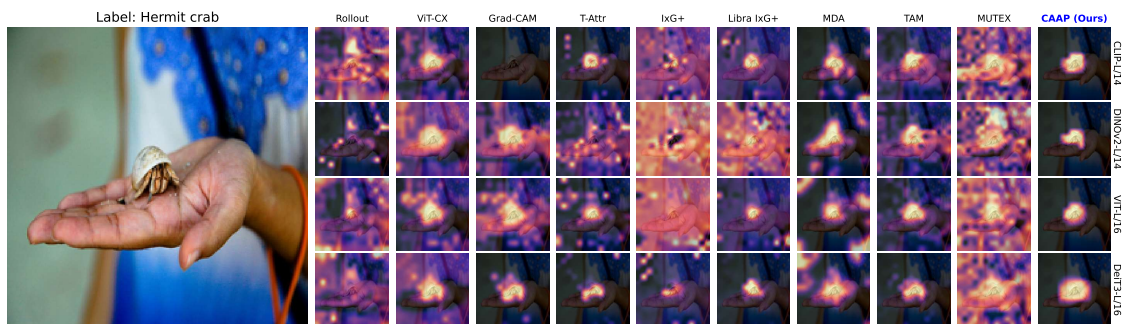


Figure 40: Visualization of attribution maps produced by different methods across various models. The target object is a Hermit crab, and our method more accurately delineates the object boundaries compared to the baselines.